LRP 744/03 January 2003

# ELM driven divertor target currents on TCV

R.A. Pitts, S. Alberti, P. Blanchard,
J. Horacek, H. Reimerdes, P.C. Stangeby

submitted for publication in
Nuclear Fusion

ISSN 0458-5895

# ELM DRIVEN DIVERTOR TARGET CURRENTS ON TCV

R. A. PITTS, S. ALBERTI, P. BLANCHARD, J. HORACEK, H. REIMERDES[1],

P. C. STANGEBY[2]

Centre de Recherches en Physique des Plasmas,
Association EURATOM-Confédération Suisse,
École Polytechnique Fédérale de Lausanne, CH-1015 Switzerland
[1]Present address: Columbia University, New York, N.Y., USA
[2]University of Toronto, Institute for Aerospace Studies, Canada

ABSTRACT

There is currently both considerable interest in the physics of ELM transport in the scrape-off layer (SOL) and concern over the impact of the ELM power and particle loads on the divertor targets of future fusion reactors. This contribution describes some experimental observations of the reaction of target floating potentials and currents during ELMs in TCV, relying principally on fast measurements of these parameters using tile embedded Langmuir probe arrays. Clear evidence is presented for rapid modifications in the local target floating potentials occurring long before the characteristic rise of hydrogenic excitation emission due to local recycling provoked by the arrival at the target of the ELM ion flux. This precursor activity appears to be synchronous with the growth of MHD modes in the main chamber. Simple conditional averaging is used to derive a "coherent ELM" and thus generate the radial distribution of the current to probes held at target potential. At some locations, the coherent ELM can also be used to estimate the time evolution of the local target electron temperature, density and power flux, even though these quantities are not directly measured. The time delays between the reactions of currents, floating potentials and derived temperature are consistent with the expectations of recently published kinetic simulations of ELM energy transport down a 1D scrape-off layer plasma. The strong potential variations observed during the ELM are the result of current flows at the targets. These currents are generally of opposite sign at inner and outer divertors and are thus consistent, at least in part, with a thermoelectric origin in which the driven current is consistent with an in/out divertor temperature asymmetry near the strike point of nearly a factor 2, probably due to the generation of divertor asymmetries by the ELM heat pulse. Such asymmetries are commonly observed in low to medium density L-modes for the particular TCV magnetic equilibrium studied in this paper. Total current balance during the ELM is satisfied only to within a factor 2, so that, whilst some of the driven current flows parallel to field lines in the SOL, there is an apparent additional negative current to the inner divertor during the ELM whose origin remains unexplained. It might, however, be due in part to increased plasma-wall interaction in the main chamber during the ELM event.

## 1. INTRODUCTION

In view of the favourable confinement obtained during H-modes in which they are present and their potential for exacting intolerable divertor damage in future tokamak reactors, Type I ELMs in particular have of late been the subject of considerable research activity [1-7]. Nevertheless, extrapolations to proposed experimental reactors such as ITER [8] remain uncertain and more reliable estimates of their likely effects, particularly with regard to divertor target erosion, require more extensive experimental measurement of key parameters and improved understanding of ELM physics.

It is the purpose of this paper to present experimental results from divertor target Langmuir probe arrays obtained during stable ELMing phases of ohmic H-modes in the TCV tokamak, illustrating an interesting ELM "precursor" in the local floating potential occurring in the vicinity of the strike points and demonstrating the presence of strong, parallel thermoelectric currents flowing in the scrape-off layer (SOL) as a consequence of the ELM. These TCV results offer strong experimental evidence for a fast electron component, coincident with the start of upstream MHD activity, arriving at the target plates before the bulk of the ELM particle deposition. They may thus be a useful tool for comparison with kinetic simulations of the ELM transport in the SOL [9].

The exact classification of the TCV ELMs obtained in the ohmic H-modes studied here remains an unresolved issue and will be discussed in the following section. Whilst there is ample evidence for a Type III character, alternative features point to a Type I classification. From the point of view of this paper, which takes as its focus the effect of ELMs on the SOL currents, the precise classification is somewhat academic in the sense that the magnitude of the observed effect is sufficient to be both of some interest and perhaps also of some concern when considering if such currents might be present in larger devices.

## 2. EXPERIMENT

To-date, the majority of H-modes in the TCV tokamak ($R = 0.89$, $a = 0.25$, $B_\varphi = 1.43T$) have been obtained with ohmic heating only [10,11], due largely to the limitation in density imposed by the X2 electron cyclotron heating (ECH) system which prevents coupling of power beyond densities of ~4 x $10^{19}$ $m^{-3}$, close to the ohmic L-H transition density. Experiments are currently underway with the newly commissioned X3 ECH system [12] extending the TCV operating space to additionally heated H-modes, but the data presented here will be restricted to

ohmic plasmas. The TCV vacuum vessel is regularly boronised and, with 90% of the first wall surface protected with carbon tiles [13], TCV can be considered an all-graphite machine.

## 2.1. Typical ELMing H-mode

The inherent flexibility of TCV allows for a large variety of magnetic equilibria to be created almost anywhere in the rectangular vacuum vessel. In fact, for reasons mostly linked to the ohmic H-mode transition, the standard operating mode of TCV has the ion $B \times \nabla B$ drift direction upwards (positive $B_\varphi$) and is hence unfavourable for the H-mode transition in single null lower (SNL) configurations. This helps to avoid the transition for a large number of experiments (notably ECH and ECCD) requiring diverted configurations both under L-mode conditions and with the main plasma in the upper half of the chamber.

A "standard" ohmic ELMing H-mode on TCV is characterised by a stable ELMing phase of duration often equal to the entire plasma current plateau phase, with the ELM onset occurring right after the L-H transition. Figure 1 presents some plasma signals acquired during a typical example of this reference discharge. The associated magnetic equilibrium may be seen in Fig. 3. At the L-H transition, it has triangularity, $\delta_{95} = 0.4$ and elongation, $\kappa_{95} = 1.65$ for $I_p = 400$ kA, corresponding to $q_{95} = 2.55$, average edge triangularity, $\delta_{edge} \approx 0.55$ and $\kappa_{edge} \approx 1.73$. Together with a line averaged density at the transition of $n_e = 5.4 \times 10^{19}$ m$^{-3}$, these values are in the middle of an empirically determined parameter range for TCV providing a gateway to this stable ELMing ohmic H-mode regime in magnetic equilibria of this type [11].

During the stable ELMing phase, at low values of $\bar{n}_e$ ($\sim 0.25\, n_{GW}$, with $n_{GW}$ the Greenwald density) such as that in Fig. 1 and for the particular magnetic geometry chosen for these experiments, ELM repetition frequencies are typically in the region of $f_{ELM} \approx 200$ Hz, $T_e(0) \approx$ 900 eV, the density profile is reasonably flat (compare $n_e$ and $n_e(0)$ in Fig. 1) and the radiation fraction, $P_{RAD}/P_{IN} \approx 0.5$, where $P_{IN}$ is the ohmic power input. These discharges are sawtoothing with sawtooth periods typically of order 120 Hz (see Fig. 2) and the ELMs provide for a relatively constant density throughout the plasma current plateau.

The magnetic configuration employed here is close to the reference equilibrium used for many edge physics experiments on TCV, notably divertor detachment experiments, the latter albeit usually conducted at somewhat lower plasma currents and in L-mode. This highly unconventional divertor geometry, combining an inner vertical target with a short poloidal X-point to target distance and a horizontal outer target with long poloidal distance to the X-point

leads also to unconventional detachment behaviour in L-mode [14]. Detachment studies in ELMing ohmic H-mode are virtually excluded in view of the restricted range of achievable plasma density. Accounting for the difference in $I_p$ in comparison with L-mode observations, at $\bar{n}_e = 0.25\ n_{GW}$, both the inner and outer divertors in the discharge of Fig. 1 are attached and probably in a regime of low recycling, at least in between the ELMs.

The use of ohmic heating alone makes classification of the ELM type according to the standard definition of ELM frequency dependence on input power [3] rather difficult. Although some "large" ELMs, expelling of the order of 10% of particle inventory and energy content are occasionally observed, typically after long ELM-free periods [10], those characteristic of long stable ELMing phases are more benign. Indeed, at $f_{ELM} = 200$ Hz, their effect on diamagnetic energy can only just be resolved. This is illustrated in Fig. 2 where signals from $D_\alpha$ emission, a central soft X-ray channel and a diamagnetic loop (DML) are compiled for the interval 0.5-0.8 s in the discharge of Fig. 1. This interval will in fact be common to much of the analysis that follows, for reasons which are explained later.

The simple technique of coherent averaging using the $D_\alpha$ recycling light intensity as reference, which will be the principal analysis tool employed in this paper (see Section 3 onwards), has been applied to the DML signal to extract the average stored energy change due to all the ELMs in the chosen time interval. The result is also included in Fig. 2, showing an average energy change, $\Delta W = 0.3$ kJ, which, when compared with the total stored energy during this interval (bottom panel of Fig. 1), yields $\Delta W_{ELM}/W \sim 1.4\%$ (note that the baseline offset on the DML signal in Fig. 2 is larger than stored energy itself - this is due simply to compensation terms which have not been subtracted from the raw data - the fractional change per ELM, which is of greatest interest here, remains valid).

The fractional power loss due to these ELMs, $(f_{ELM} \times \Delta W_{ELM})/P_{IN} \sim 11\%$, is significantly lower than the values of 30-40% typically found for Type I ELMing regimes on other devices [1]. This should be contrasted, however, with discharges characterised by similar $\kappa$, $\delta$ and $P_{IN}$, but with both divertor strike points placed on the central column tiles. In this case, for reasons which are not currently understood, the ELM frequency is lower, $f_{ELM} \sim 150$ Hz, and the corresponding ELM energy losses are higher with $\Delta W_{ELM}/W \sim 4\%$ and $(f_{ELM} \times \Delta W_{ELM})/P_{IN} \sim 29\%$, much closer to the Type I ELM scaling.

Nevertheless, the proximity of the ohmic H-mode input power to the L-H transition threshold power in these discharges, the relatively low energy loss per ELM and the observation of

coherent magnetic precursor oscillations with medium toroidal mode number near the outboard midplane (Section 2.3 and [15]) before each ELM, are strong indications for a Type III classification [3,4]. This is further supported by some very recent experiments in which an inverse ELM frequency dependence with power has been observed when X3 ECH power is coupled to an ELMing ohmic H-mode [16]. Finally, the derived divertor target power fluxes presented below in Section 4.2 are of the order of those seen elsewhere [17] during Type III ELMs.

At the time of writing, the absence of high resolution temperature and density profile measurements in the pedestal region prevents analysis of the edge plasma proximity to stability limits. An unambiguous classification of the ELM type observed in the discharges described here is therefore not possible, though new edge Thomson scattering measurements are in preparation at TCV.

## 2.2. Edge diagnostics

Langmuir probe measurements constitute the majority of experimental data reported here. As illustrated in Fig.3, two single probe arrays are installed, positioned such that for the SNL diverted configuration commonly used for edge physics studies on TCV [14] (and for the discharges described here), good coverage of the inner and outer divertor target zones is obtained. On the vessel floor, the protection tiles are flat and the cylindrical probes are of domed design with the spherical tips protruding 1 mm above the surface at the maximum of the dome. On the central column, the tiles are toroidally shaped for power handling purposes [13] and the probes are offset to one side of the toroidally symmetric contour with the tips machined to match the surface curvature. For both arrays, the probe tips have diameter 4 mm and are manufactured from the same polycrystalline graphite material as the tiles in which they are embedded. Along the flat portion of the floor (outer divertor), the 26 probe tips give a spatial resolution of 11 mm, whilst on the central column (inner divertor) the 34 probes are separated by 17.3 mm. The arrays are separated by ~90° in the toroidal direction.

In the absence of extremely fast sweeping (requiring more sophisticated electronics and great care in system design), the use of single probes in tokamak divertors generally precludes measurement of the local $T_e$ on timescales pertinent to the ELM, particularly for the relatively rapid ELMs studied here. Probe measurements during ELMs on TCV are therefore restricted to fast sampling (77 kHz)during fixed bias modes of operation (Section 2.3) giving, for an average

ELM duration of typically ~0.5 ms, around 40 data points per ELM.

A fast reciprocating Langmuir probe [18] samples the main SOL plasma at the outside vacuum vessel midplane, reciprocating through a 15 cm stroke in ≈ 200 ms. Whilst the device is designed for edge turbulence and transport studies (a similar probe has been used successfully on DIII-D to study ELM turbulence [19] and similar measurements are planned on TCV), data are presented here only for the evolution of local floating potential, $V_f$ and ion particle flux with relatively low sampling frequency (75 kHz).

The vertical line drawn through the magnetic equilibrium in Fig. 3 indicates the position of the main $D_\alpha$ photodiode viewing chord, data from which will be used throughout this paper as a general reference for the time of each ELM event (see the top traces in Figs. 1 and 2). Of note is the rather wide angle coverage of this vertical chord compared with that of an array of lateral $D_\alpha$ chords which have been omitted from Fig. 3 for clarity (they can be seen, however, in Fig. 9). Each diode signal is digitised at a frequency of 50 kHz.

Flexibility and real time control of plasma shape require a substantial number of in-vessel magnetic measurements [20]. There are currently four poloidal arrays of 38 poloidal magnetic field (Mirnov) probes installed in TCV, with fast measurements being possible on one complete array [21]. As indicated in Fig. 3, the probes are evenly distributed around the poloidal circumference and provide detailed measurements of the MHD mode structure associated with the ELM perturbation [15,21]. Data from these probes will be presented below in Section 2.4 and are particularly relevant to the apparent presence of an ELM precursor at the divertor targets.

Finally, TCV is equipped with a Heterodyne ECE system [22], with measurements possible from both the low and high field sides with high spatial resolution near the plasma edge. Results from the low field side system, available for the discharges described here and in support of the Langmuir probe data will be presented in Section 4.2.

### 2.3. Langmuir probe response, $J_{sat}$, $V_f$ and $J_0$

With the bias voltage fixed to a sufficiently large, negative value, the Langmuir probe draws the ion saturation current, a direct measure of the ion flux flowing parallel to the total magnetic field. Accounting for the probe area projected onto the field yields $J_{sat}$, the ion current density parallel to the field. The projected area requires knowledge of the total field line impact angles at the probes which, at the divertor strike points of the equilibrium in Fig. 3 are ~2.5° and

~5.5° at the inner and outer targets respectively during the plateau phase of the discharge (where the inner divertor angle also accounts for the toroidal curvature of the central column tiles). This difference in angles is due to the difference in flux expansion, $f_{exp}$, at the two targets which, near the strike points are ~4.5 and ~2 for the inner and outer divertors respectively. Poloidal magnetic field equilibrium reconstructions cannot be performed with a time resolution comparable to the Langmuir probe data acquisition rate, so that these angles are average values through the plateau phase of the discharge computed at the location of each probe and assumed to be appropriate to ELM-free and inter-ELM periods. Reconstructions over short time intervals with time resolution ~0.2 ms have, however, been performed to study the potential effects of strike point movements on the ELM timescale. The results confirm that neither field line impact angles nor strike point positions change significantly as a consequence of the ELM event.

Figure 4 compiles the time evolution of $J_{sat}$ at the inner and outer target probes, in each case for a series of 8 probes, beginning with the first probe on the private flux side of the strike point and moving progressively deeper into the SOL, or common flux region. This convention will be retained throughout the paper, such that in the case of the particular equilibrium studied here, probes 53 (inner) and 5 (outer) are in the private flux region and probes 52 (inner) and 6 (outer) are closest to the divertor strike points in the SOL. One may note that due to a gradual and uncorrected radially inward displacement of the outer divertor strike point as the discharge progresses, probe 5, initially in the outer divertor private flux region, finds itself in the outer divertor SOL for $t > 0.85$ s.

Figure 5 may be helpful in illustrating the probe positions mapped, by convention, to the outer midplane in the discharge of Fig. 4 and giving also the computed magnetic connection lengths along the field from midplane to target. The mapped probe positions and connection lengths are values averaged over the period 0.5-0.8 s.

With the exception of probes 5, 53 and 12, field lines from all members of the group of 16 probes in Fig. 4 connect around the SOL from target to target. In midplane coordinates, probes 52 and 6 are within 2-3 mm of the separatrix. By coincidence, for this particular equilibrium, characterised by a poloidally long outer divertor leg, the outer magnetic midplane corresponds approximately to one half of the target to target connection length. Within ~ 1 mm of the separatrix, midplane to target connection lengths of ~ 15 m are therefore similar for probes at both targets.

Despite the lower spatial resolution of the central column probes in comparison to those at

the outer target, the differing inner and outer flux expansions for this equlibrium (approximately a factor 2 higher at the inner target) leads to a higher effective inner divertor resolution when mapped to the magnetic midplane. In Fig. 4 and those following, data from a representative selection of those inner probes on the central column connecting to the outer target are shown for illustration.

At the top of each column in Fig. 4, the vertically viewing $D_\alpha$ photodiode signal demonstrates the stable ELMing regime obtained in this discharge, beginning at $t \approx 0.3$ s after a short ELM-free phase and terminating with a further ELM-free period just before a disruption. Although separated by more than 200 tokamak shots over a period of many days and a variety of experimental programmes, the discharges in Figs. 1 and 3 are essentially identical. During formation of the equilbrium, the outer strike point is created first on the central column and thereafter swept vertically downwards to the vessel floor. This is why the outer probe currents appear only some 300 ms into the discharge whilst the central column probes register current almost immediately after discharge formation.

One immediately obvious feature of the currents in Fig. 4, is the negative excursion seen on many of the central column probes, notably on probe 52, which is close to the central column strike point but in the SOL. At the outer target, only positive current excursions accompany the enhanced recycling events signaled by the $D_\alpha$ peaks at each ELM. For a Langmuir probe ostensibly biased into ion saturation, negative current implies that the probe operating point, or floating potential, $V_f$, is sufficiently negative with respect to the reference potential (in this case the torus potential) that the applied negative bias is insufficient to access the ion saturation current branch of the characteristic. This is in fact also observed in TCV L-mode discharges in which, at low to medium $\bar{n}_e$, probes in the vicinity of the central column strike point may sometimes adopt large negative $V_f$ when the $B \times \nabla B$ drift is directed away from the X-point in SNL equilibria (see Figs. 23, 24 at the end of this paper). That $V_f$ is always positive at the outer target in the same discharge is a strong indication of the passage of parallel thermoelectric currents [23] driven by the target temperature asymmetry characteristic of most tokamak divertors. Following a demonstration in Section 4 that thermocurrents may be at the origin of the ELM driven current, Section 5 will turn to an L-mode plasma as an illustration of the general presence of parallel currents in TCV.

By removing the connection to the external bias circuit, the probe floating potential may be measured on a fast timescale in a separate, but identical discharge. Figure 6 presents an

example for the same probe numbers as in Fig. 4. Evidently, the negative current spikes in the $J_{sat}$ of some central column probes are a consequence of the large negative excursions in $V_f$, particularly on probes near the inner strike zone. The amplitude of these events often exceeds the bias voltage applied to the probe during $J_{sat}$ collection, typically in the range of -100V. Of note also are both the large positive $V_f$ spikes at each ELM near the outer target strike point, and the appearance, deeper in the SOL, of negative $V_f$ spikes at the outer target too. At the inner target, negative spikes are present on all probes, but positive excursions also accompany the ELM event for probes deeper in the SOL. Clearly, the ELMs drive rapid and complex rearrangements of potential in the target vicinity.

In TCV, each graphite first wall tile is bolted to the vacuum vessel in a single location. There are usually guiding surfaces providing differing degrees of contact, but all tiles are in principle directly electrically connected to the vessel wall in at least one location. Since the divertor target potential should thus remain fixed at the torus potential (approximately zero volts), any change in $V_f$ implies that the potential between the plasma and the target must also have changed. Even for rapid changes, the probe current density at zero applied voltage, $J_0$, should change on the same timescale as $V_f$, since it is largely dependent on the electron current arriving at the probe. It is also a direct measurement of the local current density flowing into (or out of) the target tiles.

Figure 7 illustrates the evolution of $J_0$, in a third separate, but similar ELMing discharge (actually the discharge from which the plasma signals in Fig. 1 are obtained). As expected, the probe currents behave qualitatively in similar fashion to the $V_f$ signals in Fig. 6. Defining a current flowing from the SOL to the target as positive, Fig. 7 implies a net electron current flow from *outer* to *inner* targets during the ELM, at least in the strike point vicinity. For the discharges discussed here, the plasma current is, like that of $B_\varphi$, directed counterclockwise when viewed from above. Note that $J_0$ in Fig. 7 is given as a parallel field current density (as for $J_{sat}$) in units of $Acm^{-2}$ and that at the outer target it is of similar magntiude to $J_{sat}$. Near the the inner target strike point, for the bias potentials available on the TCV probes, the rapid fall in $V_f$ at the ELM prevents an adequate measurement of $J_{sat}$ there for comparison with $J_0$.

## 2.4. MHD activity and SOL/Divertor ELM precursors

Coherent magnetic oscillations usually preceed the ELMs characteristic of the discharges described here. Their structure has been studied in some detail and has been found, in many

cases, to comprise an early toroidally localised, medium toroidal mode number (n = 7 - 9) precursor often occurring some 0.1 ms before the $D_\alpha$ recycling signal begins to rise [15,21]. The mode grows in toroidal extent and amplitude until the entire toroidal circumference is encompassed, at which point the enhanced phase of particle and energy transport characterisitic of the ELM begins. A strong n = 5 component, associated with high poloidal mode numbers, often appears to be responsible for the rapid growth in mode amplitude during the later phase of the precursor activity before the onset of the ELM. Unfortunately, a recent modification of the TCV Mirnov coil system, required for plasma control purposes, has reduced the effective probe area by a factor of ~ 3.5 such that detection of the weak higher n precursor components is no longer possible, although the later, larger amplitude phase of the magnetic precursor remains accessible.

An example of the poloidal mode structure of the precursor is given in Fig. 8 which compiles magnetic and Langmuir probe data from the discharge featured in Fig. 6. To the left of the figure, the full time evolution of the signals is illustrated, repeating the $V_f$ data from target probes 52 and 6, closest to the inner and outer strike points and now including the time derivative of the poloidal magnetic field from the triplet of Mirnov coils 17, 18 and 19 located on the low field side, acquired at a sampling frequency of 1 MHz and symmetrically distributed about the magnetic axis of the equlibrium (see Fig. 3). Also included are the parallel ion saturation current density and local floating potential from the reciprocating Langmuir probe inserted up to the separatrix radius at 0.6 s. On the right of Fig. 8, a single ELM has been selected near the peak of the fast probe reciprocation and the traces expanded appropriately.

It is immediately obvious that the three floating potential traces, one at each divertor target and the third from the main chamber SOL apparently react to the ELM long before any sign of enhanced recycling (top $D_\alpha$ trace) or magnetic precursor activity. The magnetic oscillation occurring around 598.35 ms is not associated with the ELM (this ~80 kHz perturbation has the same phase and equal amplitude on all probes and is likely due to resonance in the probe amplifier chain). As the $D_\alpha$ emission begins to rise (the region between the two vertical dashed lines in the right column), there is a change in the gradient of the $V_f$ time response, the fast probe $J_{sat}$ begins to oscillate strongly and there is clear mode activity at around 60 kHz on the Mirnov coils. No such oscillation is seen on the three coils located at the same vertical positions on the HFS, nor is any perturbation visible on LFS neighbouring coils 16 and 20. Note that of the three coils, the signal on coil 18, at the midplane and closest to the plasma, is largest. The perturbation

is therefore extremely localised at the outside midplane of the equilibrium, consistent with findings elsewhere [24] in double null configurations. As an interesting corollary to these TCV measurements, it is also notable that the ELM induced $J_{sat}$ spikes on the fast probe pins persist at high amplitude even when the probe is close to the wall radius ($R_{wall}$ ~ 23 mm in midplane coordinates - see lower left panel to the right of Fig. 8). This has also been recently observed on the MAST tokamak [25] and suggested as being associated with the fast radially outward motion of a toroidally or poloidally localised structure, possibly resembling the ballistic movement of plasma "blobs" or current filaments now being increasingly held responsible for turbulent losses in the plasma edge [26].

Analysis of the mode structure using the pitch angle of the field lines on the 95% flux surface yields a poloidal mode number, m ~ 13. Since $q_{95}$ ~ 2.55 this is consistent both with a resonant pertubation close to the plasma edge having toroidal mode number n ~ 5, and with previous magnetic precursor measurements during ELMs alluded to at the beginning of this section. As such, there is no reason to believe that the toroidally asymmetric precursors present during those earlier measurements no longer occur and it would thus appear reasonable to suppose that the early response of SOL potentials with respect to the onset of the ELM proper is linked to this magnetic precursor activity. With respect to timescales, the SOL $V_f$ precursor always begins some 0.1 ms before the onset of the later phase of coherent magnetic activity and would therefore be in reasonable synchronisation with the start of the early toroidal magnetic precursor.

Concerning the $V_f$ precursor itself, one possible reason for a negative dip in floating potential can be the presence of even a small population of fast electrons in the particular magnetic flux tube terminating on the probe [27]. This would not, however, explain the positive excursions seen on both the fast reciprocating probe pin and the outer divertor strike point probe. It is also notable that the fast probe enters the SOL below the magnetic midplane and is thus on the outer divertor side of the SOL stagnation point.

Thermoelectric currents were already mentioned briefly in Section 2.3 and can be readily responsible for modifications to the local plasma potential. Such currents require the development of $T_e$ asymmetries which cannot yet be directly measured in TCV on the ELM timescale with the available diagnostics. Sections 3 and 4 will address in more detail the question of thermoelectric currents by using a simple averaging technique to extract an "average ELM" at the target plates.

## 3. THE AVERAGE ELM

Coherent averaging of repetitive complexes in a signal as a means of reducing noise is a well established and simple statistical technique. It is particularly appropriate to tokamak ELMs in the sense that a specific marker signal, in the form of the $D_\alpha$ spike associated with enhanced recycling due to the ELM at a specific location, can be reliably identified. Assigning the peak in the $D_\alpha$ intensity for a given viewing chord to the zero of a new timebase for each ELM allows all the members of a group of ELMs on a given signal and within a given time interval to be summed and averaged, yielding a single, "coherently averaged" ELM. This simple approach has in fact already been applied to analysis of divertor Langmuir probe signals from both the JET and ASDEX-Upgrade tokamaks [28,29]. It was used to compute an average plasma stored energy loss per ELM in Section 2.1 (Fig. 2).

The relatively uniform ELMs characteristic of the discharges described here are well suited to the coherent averaging method. Their frequency is sufficiently constant that a well defined period on either side of the reference time can be chosen and fixed. For all cases presented below, an interval of 2 ms on each side of the $D_\alpha$ reference signal peak has been used to constitute the average, yielding 310 and 200 points per coherent ELM for the Langmuir probe and $D_\alpha$ signals respectively. Concerning the time interval during the discharge over which the ELMs are averaged, this is chosen such that the problems associated with the outer strike point movement mentioned earlier and responsible for the changes after ~0.85 s on the $J_{sat}$, $V_f$ and $J_0$ signals of probe 5 in Figs. 4,6,7 are avoided. During the plasma current plateau phase of these discharges, the strike point moves a distance of ~1.4 cm inwards. This is comparable to the outer target Langmuir probe separation. During the first 400 ms following formation of the complete equilibrium (at 0.4 s), the drift is slower, ~3 mm, corresponding to ~1 mm at the outside midplane. In what follows, the period 0.5-0.8 s has thus been chosen for the averaging interval, corresponding to a total of ~60 ELMs.

### 3.1. $D_\alpha$ emission

Although the burst of $D_\alpha$ emission provoked by the ELM is in general a good marker with which to distinguish when the particles associated with it have made their way to various surfaces, the temporal behaviour and amplitude of the intensity can be very dependent on where the observations are made and on the particular magnetic and machine configurations. This is illustrated in Fig. 9 in which the coherently averaged ELMs from the discharge in which the $J_{sat}$

data in Fig. 4 were obtained are presented for the 10 $D_\alpha$ lines of sight (LOS) available on TCV. The inset at the top left shows the LOS superimposed on the magnetic equilibrium, together with an idea of the approximate poloidal extent over which light is collected by the lateral photodiodes. As noted in Section 2.2, the angular divergence is very much greater for the vertical diode (channel #1). In addition, this vertical LOS diode is unapertured and thus yields a considerably greater signal than its horizontal counterparts.

These photodiodes are uncalibrated but can still be directly compared with respect to time dependence during the ELM and to some extent also in absolute magnitude (the latter at least for the lateral diodes which all have the same aperture diameter in front of the detector - note that the amplitude of the signals on diodes #2-10 has been multiplied by 10). In Fig. 9, as for the remaining figures, the coherent average timebase is computed with reference to the vertical LOS, such that t = 0 corresponds to the peak in the ELM signal on this channel. Very different time evolutions in the coherent ELM characterise the response of the various LOS, particularly channels #7,6,5 for which the LOS progressively encroach on the X-point region from above. In these cases, the response is more smeared out in time and even double peaked structures are observed. The first of these peaks, in common with the single peaks noted on the signals from the lower three LOS, intersecting the long outer divertor leg, appear to occur slightly earlier than that on the vertical diode.

Understanding the behaviour of these diode signals even semi-quantitatively is extremely difficult. One might interpret the appearance of a peak earlier in time (than the signal on the vertical diode) on those signals viewing the divertor areas as indicative of the arrival of particles expelled by the ELM at the divertor targets, but the likely interaction, to some extent, of the ELM with all wall surfaces complicates the interpretation of the relatively delocalised recycling intensity. It does appear, however, that upon closer inspection, the ELM causes all diode signals, including the vertical LOS, to react approximately simultaneously (within several 10's μs). This being the case and considering that there is no LOS viewing exclusively an area of either divertor, the vertical channel will henceforth be used as the reference signal for coherent averaging. It can be thought of as an effective average of the behaviour of all channels. With regard to time delays between Langmuir probe signals and this $D_\alpha$ reference, Fig. 9 shows that these values will be ~20 μs longer than would be the case had any of the lateral channels (#8,9,10) been chosen instead.

Figure 10 demonstrates how the coherent ELM generated from the vertical LOS is a very

reasonable representation of all the ELMs in the chosen averaging period of 0.5-0.8 s. Relative standard deviations for the ELM amplitude and area under each ELM (with respect to the coherent ELM) are 11% and 4.5% respectively. The variation in ELM frequency is slightly higher at 14.3% for this sample. These numbers differ little when extending the averaging period over the entire stable ELMing phase (~ 600 ms).

### 3.2. Langmuir probe response, $J_{sat}$, $V_f$ and $J_0$

For the same time interval (0.5-0.8 s) and for the same target Langmuir probes, Figs. 11-13 are the coherently averaged analogs of Figs. 4,6,7 respectively. As before, the signal from the vertically viewing $D_\alpha$ diode is included for reference. The extent to which these coherent target probe ELMs may be considered representative of any individual ELM is discussed later in Section 3.2.1. Of course, whilst the averaged data broadly reflect the trends noted in the full time traces of Figs. 4,6,7, the averaging helps to identify a number of interesting aspects of the target response to the ELM. When comparing absolute magnitudes, particularly of probe currents (Figs. 11, 13), it is important to recall that these are current densities parallel to the total magnetic field. Proper current balance (Section 4.4) accounts for field line geometry in projecting currents onto the divertor targets.

As in the case of the individual ELM example of Fig. 8, the coherent averages near the strike points clearly show a reaction to the ELM before the $D_\alpha$ intensity begins to rise. This will be discussed in more detail in Section 4.1. In general terms, a negative excursion in $J_0$ (and to a lesser extent in $V_f$) at one target is accompanied by an opposite trend at the other, though the probe numbers at the inner and outer targets in the left and right columns of Figs. 11-13 do not correspond directly in terms of midplane separatrix distance (see Fig. 5 for an approximate correspondance). This is already an indication that parallel current balance might at least be approximately satisfied during the ELM itself, at least in parts of the SOL where the majority of the current flows - Section 4.4 will address this key result further.

It has already been noted in Section 2.3 that the large decrease in $V_f$ near the inner strike point compromises the measurement of $J_{sat}$ there given the limited experimental probe bias potential. This is evident in the *decreases* in $J_{sat}$ on all inner target probes coincident with the dips in $V_f$ occuring during the $D_\alpha$ rise, even deep into the SOL. Nevertheless, provided the local $T_e$ rise during the ELM deeper into the divertor SOL is not too high, as the $V_f$ recovers after the $D_\alpha$ peak, the applied bias voltage (-100 V) should be sufficient to ensure that the probe draws the

ion saturation current. It is thus probable that the time evolution of the $J_{sat}$ coherent averages on inner target probe numbers 50-40 (Fig. 11) can be interpreted with some confidence as representative of the true saturation current. With this in mind, comparison of the coherently averaged $J_{sat}$ on inner and outer target probes deeper in the SOL reveals a rather similar time evolution, with the currents reaching their maximum values some 100 μs after the peak in $D_\alpha$. With regard to an interpretation of the measured edge currents in terms of thermoelectric effects, it is comforting to note that where $J_{sat}$ can be taken as the true value, its magnitude is always greater (though not always by much) than that of the corresponding $J_0$, the current at zero probe bias.

These coherent averages also help to emphasise the tendency, already visible in Figs. 6,7, for a very large floating voltage and accompanying strong current in the inner private flux region compared with a much lesser effect at the same location on the outer target (cf. probes #5, 53). This observation will be further discussed in Section 5 in relation to similar effects commonly noted in L-mode plasmas. In the SOL itself, the detailed time evolution during the ELM of $V_f$ and $J_0$ is extremely complex and is likely beyond simple interpretation.

3.2.1 Target signals: coherent versus individual ELMs

Figures 14, 15 illustrate the extent to which the coherent ELM is truly representative of any individual event. In Fig. 14, all the ELMs in the now familiar interval 0.5-0.8 s are plotted along with the coherent ELM for the two probes nearest the inner and outer strike points and in each case for the three probe modes of operation. There is greater scatter around the mean value than for the $D_\alpha$ signal, though there is no straightforward way to quantify the statistical variation. Similar trends are observed for the other probes comprising the target arrays. There is a general tendency for larger fluctuations from the mean at the ELM peak.

Figure 15 is analogous to Fig. 14, but comparing individual, randomly selected ELMs from the three separate discharges (corresponding to the three probe operation modes) with their coherent averages. Large fluctuations are evident in all traces so that individual departures from the coherent ELM can be significant from ELM to ELM. The time resolution of these measurements is insufficient to fully characterise the turbulence, but the relative fluctuation level in between and during the ELMs is similar. More quantitative experiments on the turbulent nature of particle fluxes and electric fields during the ELM are planned on TCV, similar to the recent work reported from DIII-D [19]. In contrast to observations during ASDEX-Upgrade

Type I ELMs [29], strong turbulent phases during the ELM rise time are not generally observed in TCV on the coherently averaged, nor individual $D_\alpha$ or $J_{sat}$ signals, at least at the outer target where the ion flux measurements are not compromised by the strong negative floating potential variations. Such turbulence is likewise not observed during JET Type I ELMs. There is some evidence, however, for higher fluctuation levels in the main SOL ion flux in TCV during the ELM rise (see Fig. 8).

3.2.2 Target ELM precursors

The early response, particularly on the floating potentials of probes #52 and #6 near the inner and outer strike points respectively was already evident in the individual ELM of Fig. 8. Recourse to the $V_f$ coherent averages in Fig. 12 illustrates the effect more clearly. For clarity, the coherent ELMs for these probes in both $V_f$ and $J_0$ have been extracted from Figs. 12, 13 and are replotted in Fig. 16 along with the usual averaged vertical $D_\alpha$ ELM.

The coherent ELM on $V_f$ highlights this "precursor" activity, in particular showing a double feature in the time response - a slower rise beginning ~250 μs before the $D_\alpha$ begins to react and a faster rise coinciding with that of the $D_\alpha$, the latter clearly linked to the rapid changes in $J_0$ (and, more correctly, $J_{sat}$) accompanying the rise in recycling emission. The shoulder in $V_f$ on the outer target probe is slightly less visible than for its inner target counterpart. Section 2.4 has already described how magnetic measurements on TCV have previously identified the presence of a toroidally localised precursor oscillation during ELMs, occuring several 100 μs before the onset of the increased transport phase manifest in the $D_\alpha$ emission. These timescales are of the correct order to explain the $V_f$ response and are suggestive of the release of fast electrons into the SOL before the fully turbulent stage of the ELM develops.

Whilst the early decrease in $V_f$ on Probe #52 is also evident on $J_0$, the current to Probe #6 near the outer strike point does not likewise appear to respond to the clear increase in floating potential noted on this probe before the $D_\alpha$ ELM begins. This is rather difficult to understand, since, as Section 2.3 has remarked, any change in $V_f$ reflects a change in the local plasma potential which in turn must affect $J_0$. Inspection of the $J_0$ response of Probe #6 for a number of randomnly chosen individual ELMs reveals similar behaviour - the local target current near the outer strike point does not appear to respond to the $V_f$ excursion. It is also worth noting that the response of $J_0$ to changes in $V_f$ is consistently observed throughout the inner divertor SOL, but never at the outer. In the absence of any straightforward physics reason why this might be so,

one may speculate that the differences may be linked to hardware differences between the probe arrays (Section 2.2). The inner probes are flush mounted, though in a toroidally shaped tile, whilst the floor, or outer target array, is comprised of domed probe tips in a flat tile. Though field line incidence angles are slight (~ 2° at the inner target strike point), there is no reason to expect a serious impact on probe interpretation.

Regarding the timescale for particle transport along field lines from the outside magnetic midplane (where the MHD analysis (Fig. 8) clearly shows the ELM to originate), ions complete the journey in a time, $\tau_{\|} = L_c/c_s$ with $L_c$ the parallel connection length along field lines from midplane to target and $c_s = \sqrt{e(T_{e,ped} + T_{i,ped})/m_i}$ is the sound speed ($T_{e,ped}$, $T_{i,ped}$ in eV) evaluated for these approximative purposes at the top of the H-mode pedestal [1].

With the exception of ECE measurements, for which caution must be exercised in interpreting absolute $T_e$ values for edge channels (Section 4.2), only the Thomson Scattering system on TCV provides some indication of the pedestal temperature. The standard laser repetition rate (50 Hz) of this diagnostic is insufficient to yield ELM-resolved information, but averaging the radial profile across the discharge through ELM and ELM-free periods indicates a pedestal $T_{e,ped}$ ~ 100 eV. For $L_c$ ~ 15 m just outside the separatrix (Fig. 5), assuming $D^+$ ions and $T_{i,ped} = T_{e,ped}$ gives $\tau_{\|}$ ~ 150 μs. This is in approximate agreement with the timescale of the early part of the $V_f$ evolution near the strike points, before the target current itself begins to grow (positively or negatively, depending on the strike point). In contrast, the thermal speed of electrons in a Maxwellian velocity distribution characterised by a 100 eV temperature will carry them to the targets in ~ 3 μs, essentially instantaneously on the ion transit timescale. Though direct comparisons are not possible, these observations are not inconsistent with recent particle-in-cell (PIC) simulations of ELM energy transport in the SOL due to Bergmann [9], demonstrating how the hot electrons expelled by the ELM travel quickly to the targets, establishing a new sheath voltage drop and locally increasing $T_e$ (see also Section 4.2), only for the slower ion heat pulse to arrive later (by some 20-40 hot electron transit times) on the timescale of the sound speed computed for the higher, ELM induced, temperature. Section 4.2 will return to this subject.

## 4. WORKING WITH THE COHERENT ELM

Armed with the averaged target response and supposing that it is a reasonable representation of any given individual ELM, the data can now be used to look more carefully into the nature

of the currents that are evidently driven by ELMs on TCV. The coherent average can also be employed to extract useful additional information from the probe signals pertaining to a general ELM, even when, by necessity, the original data have been obtained in separate tokamak discharges.

## 4.1 Particle flux profiles

It is of considerable practical importance to ascertain from current experiments whether or not ELMs in a next step machine would be expected to broaden the power deposition profile on the divertor targets. It appears, at least from studies performed so far using Infra-Red thermography of divertor targets in JET and ASDEX-U, that this does occur to some extent but that the profile may at most be a factor 2 broader during the ELM than in the ELM-free phases [30]. At least at the outer target in TCV, where the $J_{sat}$ measurements are not perturbed by strong negative $V_f$ excursions during the ELM, the coherent ELM can be used to reconstruct the target ion flux profiles throughout the ELM duration. Whilst this is not the power flux itself, the ion particle flux is directly proportional to the heat flux density crossing the target sheath [23]. Furthermore, the kinetic simulations of the SOL energy transport due to an ELM heat pulse cited in Section 3.2.2 have clearly shown that most of the energy is delivered to the sheath by the ions provided secondary electron emission at the target plates is not important [9].

Using the $J_{sat}$ coherent averages in Fig. 11, ion flux profiles across the outer target for various times during the ELM have been compiled in Fig. 17. The data are mapped to the outside midplane with the computed magnetic coordinates averaged over the period 0.5-0.8 s. For clarity, the time of each profile is indicated by the dashed vertical lines on the coherently averaged $D_\alpha$ ELM at the top of the figure. Signals from all the probes in Fig. 11 have been included even if field lines on probes #11,12 do not connect from target to target (Fig. 5).

With the exception of the two examples at t = -0.04 and -0.08 ms during the $D_\alpha$ rise time, the profiles are reasonably exponential. Already at the ELM peak (t = 0 ms), the profile is only slightly steeper in comparison to that measured some 1.5 ms before the ELM (marked as "Before ELM" in Fig. 17). One may also note that the monotonic nature of the profiles both in the ELM-free period and during the ELM itself is strongly suggestive of an attached divertor plasma.

The characteristic e-folding distances for these profiles are of the order 8 mm in midplane coordinates. During the rise time of the recycling intensity, the ion flux profiles are steeper and

exponential only in the near SOL with e-folding distances approximately a factor of 2 shorter. It thus appears that, as seen elsewhere for heat flux [30], the spatial profile shape of ion flux is largely preserved during the ELM, with the major consequence of the event being to increase the amplitude of ion flux across the target by a large factor (an order of magnitude for the ELM discussed here). As noted in [30], if cross-field transport is Bohm-like, the relative invariance of the ELM profile shape may be a consequence of an increased diffusive perpendicular transport being offset by a reduced SOL parallel transit time, both effects being due to an ELM-induced increase in edge $T_e$ (see Section 4.2).

## 4.2 Target $T_e$ and power flux during the ELM

Even at the fastest sampling and sweep rates possible on the TCV divertor single Langmuir probe diagnostic, the ELM duration and frequency is far too rapid for meaningful $T_e$ measurements to be possible during the ELM itself. However, if the coherent averages for $J_{sat}$, $J_0$ and $V_f$ from separate, very similar discharges, can be taken as representative of the parameters that would be measured in the same discharge if all operational modes were simultaneously possible, then the standard expression for the strongly magnetised Langmuir probe characteristic [23] can be used to extract $T_e$. Thus, for $T_e$ in energy units (eV),

$$J = J_{sat}(1 - \exp((V - V_f)/T_e)) \tag{1}$$

with V and J the applied voltage and probe current respectively. Imposing the condition, as in experiment, of V = 0 yields an expression for $T_e$:

$$T_e = V_f/\ln(J_{sat}/(J_{sat} - J_0)) \tag{2}$$

which, since the coherent averages are all referenced to the same ($D_\alpha$) timebase, is readily computed. An example result appears in Fig. 18 for probes #6,7 nearest the strike point in the outer target array. Similar analysis cannot be performed for many of the inner target probes owing to the $J_{sat}$ perturbation due to the very negative $V_f$ there during part of the ELM. Once $T_e$ is known, it can be combined to yield the local density: $n_e = J_{sat}/ec_s$ and the target power flux: $P_\perp = \gamma J_{sat} T_e \sin\alpha$ with $\gamma$ the sheath heat transmission coefficient ($\gamma = 7$ assumed, see [23]) and $\alpha$ the incidence angle between the total magnetic field and the target surface. Both $n_e$

and $P_{\perp}$ are also included in Fig. 18.

Interestingly, the early reaction of $V_f$ near the outer target strike point (see also Section 3.2.2), leads, via eqn. (2) to a computed $T_e$ which anticipates the ELM and peaks before the $D_\alpha$ rises. The predicted value increases by approximately a factor 1.7, some 100 μs before the $D_\alpha$ peak, but the signal is noisy due to the logarithmic term in eqn. (2) and the proximity of $J_{sat}$ and $J_0$. One probe further out in the SOL, corresponding to about 4 mm at the midplane (see Fig. 5), the inferred $T_e$ is lower pre-ELM, rises slightly later and reaches similar peak values. If this estimated $T_e$ can be assumed reasonable, the maximum value of ~50 eV implies that ion saturation will only just be attained for the maximum applied negative bias of -100 V.

Electron temperature behaviour of this type has also been seen at the outer target with Langmuir probes during Type I ELMs in JET [28,30], though on this occasion using coherent averaging on triple probe measurements yielding the $T_e$ directly. In JET, the $T_e$ rise is larger (~ 2.3x the pre-ELM value) but the peak in $T_e$ occurs, as in TCV, some 100 μs before that in $J_{sat}$. Comparison can only be qualitative, owing to the very different H-mode conditions, magnetic geometry, machine size and opposite BxVB drift direction, but the results from both machines are qualitatively consistent with a pulse of hotter electrons reaching the target plates before the bulk of the ion energy arrives. In neither case does the local $T_e$ appear to reach the extremely high values predicted by the Bergmann modelling, but it is unclear that the very short predicted timescales (a few hot electron transit times - see Section 3.2.2) over which the temperature increase occurs would be resolved by the probe. More refined PIC simulations by Tskhakaya [31] have also recently demonstrated how the self-consistent incorporation of recycling neutrals can have a significant effect on, for example, the time evolution of the divertor heat flux.

The only other alternative measurement of $T_e$ in the boundary region on TCV is provided by the ECE diagnostic. Intepretation of this data near the edge, where optical depths are on the limit of being semi-transparent, is fraught with difficulty and it is therefore extremely difficult to assign an absolute value to the temperature corresponding to the strength of any given ECE emission. For one of the discharges discussed in this paper, #20703, the TCV second harmonic, ECE super-heterodyne radiometer [22], was configured to monitor X-mode emission from an antenna located on a LFS equatorial port, ~ 23 cm below the magnetic axis of the equilibrium, although the radiometer channels correspond to frequencies for emisison located on the HFS. The signals from channels closest to the separatrix show clear bursts synchronised with the ELM $D_\alpha$ events. An example is presented in Fig. 19, for the channel whose frequency (108.6

GHz) corresponds to a vertical emission layer practically superimposed on the separatrix (which is essentially vertical on the HFS for this equilibrium - see Fig. 3). For comparison with the Langmuir probe data, this ECE emission has also been coherently averaged in the standard 0.5 - 0.8 s time window.

Although the ECE data acquisition frequency in this case was only 20 kHz, this is sufficient to detect a slight tendency, as with the Langmuir probe estimated target $T_e$, for the effective radiometer temperature, $T_{rad}$, to peak earlier than the reference $D_\alpha$ signal. With regard to absolute value, $T_{rad}$, cannot, unfortunately, be interpreted as a true measure of the local $T_e$. Strong refraction due to the LFS position of the ECE antenna and the relatively high $n_e$ (for the TCV radiometer) means that radiation is collected only after multiple reflections in the vacuum chamber. In addition, the edge plasma at the emission layer is semi-transparent ($\tau \sim 1$, with $\tau$ the optical depth). This, together with the fact that the ECE radiometer is calibrated by normalisation to the Thomson scattering data in the L-mode, limiter phase of the discharge, implies that the inter-ELM $T_{rad}$ probably overestimates the local $T_e$. Assuming Maxwellian electrons, the relative increase in the ECE signal during the ELM is due mainly to the combination of the true $T_e$ variation in the emission layer and the variation in the optical depth through both changes in the separatrix $T_e$ and $n_e$ ($\Delta\tau \propto \Delta T_e/T_e + \Delta n_e/n_e$), neither of which are of course known. Some indication that the ECE intensity might be strongly affected by the ELM provoked local density change is provided by the shape of the time evolution of $T_{rad}$ in Fig. 19. This is very similar to the time dependence on lateral photodiode channel #7 in Fig. 9, the viewing chord of which intersects the approximate region from which the ECE emission originates (although the effects of refraction make it difficult to specify with confidence the spatial location of the emission).

Regarding the power flux density, given in Fig. 18 as the value projected onto the target, the values are comparable to those found using IR thermography of target plate surfaces in ASDEX-U during Type III ELMing discharges when, for $I_p = 600$ kA and with 1.4 MW of RF power, the peak ELM power deposition on the outer target reached 12 $MWm^{-2}$ [17]. At TCV, the Langmuir probe data shows that a 400 kA plasma current in an ohmic H-mode yields ~8 $MWm^{-2}$ at the peak of the ELM pulse just outside the separatrix. Most of this power flux originates from the ion component, in agreement with the expectations of PIC modelling. At the ELM peak, the estimated local target electron density has risen by an order of magnitude in comparison to its pre-ELM value.

One might expect the strong measured current flowing during the ELM to influence the target power flux density via a modification to the sheath potential fall and hence the sheath heat transmission [32]. It has been shown [33], however, that the heat flux onto the surface is only a relatively weak function of the normalised (to the local $J_{sat}$) current. In fact, compared to the case when $J_0 = 0$, if no correction is applied for the current flow (as for data in Fig. 18) the target heat flux density is actually slightly underestimated.

It is instructive to compare the energy, $W_\perp$, deposited on the target by the inferred ELM power flux density with that expected on the basis of the average stored energy lost per ELM, estimated in Section 2.1. Assuming for simplicity a square wave pulse of duration $\tau_{ELM}$ ~200 μs and with amplitude $A_{ELM}$ ~5 $MWm^{-2}$ (a reasonable average value for the computed ELM power pulse in Fig. 18), over an area corresponding to a single e-folding distance (~8 mm (Fig. 17) at the outer midplane corresponding to $d_{ELM}$ ~20 mm on the target for a flux expansion of 2.5 near the strike point), one expects at the outer target, $W_\perp \approx 2\pi R A_{ELM} \tau_{ELM} d_{ELM}$ ~ 100J for R = 0.75 m corresponding to the outer strike point major radius.

Returning to Fig. 2, the coherently averaged DML signal suggests stored energy loss per ELM of ~ 300 J for these 200 Hz ELMs. The above estimate from the Langmuir probe data is clearly therefore consistent with midplane energy loss given that the latter must be divided between two targets. In fact, at other facilities, where such measurements are possible, it appears that as much as half the midplane energy loss is unaccounted for at the targets [30]. Furthermore, it may also be the case that the ELM power is preferentially deposited on one particular target (see below).

### 4.3 Thermoelectric currents

Having estimated a local outer target $T_e$ from the coherent ELMs in $J_{sat}$, $V_f$ and $J_0$ and having some evidence for an increase in the main chamber SOL $T_e$ during the ELM, it is instructive to investigate if thermoelectric effects, of which the data are strongly suggestive, could be responsible for the observed Langmuir probe currents. Unfortunately, the incompleteness of the experimental data, notably the lack of direct measurements of temperature at both targets, prevents quantitative analysis that would constitute direct proof. Nevertheless, the available data can be used to address the question of what asymmetry in target temperatures would be required to account for the measured target currents assuming a purely thermoelectric origin.

These parallel (to the total magnetic field) currents, first predicted by Harbour [34], then

observed on JET and elsewhere [35-38] are driven by differences in the sheath potential fall at the surfaces intersecting the ends of a an open magnetic field line for which the electron temperatures at each end are unequal. For grounded divertor plates at each end of the connecting SOL (as in the TCV case described here), a positive thermoelectric current should flow out of the target where $T_e$ is higher and into the colder target (so that the electron current is in the opposite direction - from the cold to the hot end). Staebler and Hinton [32] have extended the original theoretical model of Harbour [34] to include finite thermal conductivity in the connecting SOL plasma and offer the following expression for the net parallel current density:

$$\hat{J}_{||} = \frac{\bar{\sigma}_{||} T_c}{L_c} \left\{ \kappa(r_T - 1) + \ln\left( \frac{(1 + \hat{J}_{||})}{(1 - \hat{J}_{||} r_T^{1/2})^{r_T}} \right) \right\} \qquad (3)$$

where $r_T = T_h/T_c$ is the ratio of electron temperatures at the two ends of a field line along which the normalised current density, $\hat{J}_{||}$ flows and where the subscripts c,h denote "cold" and "hot" respectively. Normalisation of the parallel current is made with respect to the ion saturation current density at the cold end, $\hat{J}_{||} = J_{||}/J^c_{sat}$, $L_c$ is the connection length along the magnetic field from target to target, $\bar{\sigma}_{||}$ the averaged parallel electrical conductivity along the field line and $\kappa = (0.5\ln(2m_i/\pi m_e) + f_{PSE} - 0.71)$, where $f_{PSE}$ is a factor giving the magnitude of the presheath potential drop and is model dependent. Its value can be in the range ~0.7-0.9 [23], so that $\kappa$ is a number of order 4.

Equation 3 is derived assuming that parallel pressure balance is satisfied along the field line (no target to target parallel pressure gradient). Although the equation can easily be extended to include pressure imbalance [36], the latter cannot be estimated from the available data and so the term is omitted here. It will make an important contribution to $\hat{J}_{||}$ only in the case that $T_h \approx T_c$, the opposite of the situation supposed in attempting to estimate the $T_e$ asymmetry responsible for the driven current. Indeed, even if a parallel pressure gradient were present along the SOL, it is unclear what form to assume for it. Similarly the main uncertainty in applying eqn. 3 resides in the unknown value for $\bar{\sigma}_{||}$, which can only strictly be computed if the full parallel $T_e$ profile is available. Here, the unconventional TCV divertor geometry is unhelpful in providing potential for reasonably strong parallel gradients at even relatively low density [39], though neither measurements nor simulation exist for H-mode conditions. As an approximation, Spitzer conductivity is assumed with $\sigma_{||} \approx 3.6 \times 10^7 T_e^{3/2}$ ohm$^{-1}$m$^{-1}$ ($T_e$ in keV) and, following

[36], $T_e = T_h$ to avoid overestimating the high conductivity in the main chamber SOL and underestimating the lower values near the divertor separatrix. Of course, this latter assumption is made on the implicit expectation that there is indeed a target $T_e$ asymmetry as evidenced by the large experimental currents detected (though the current could also be a consequence of strong pressure imbalance). For the connection length, $L_c = 30$ m is assumed as the target to target distance roughly corresponding to the radial position of probe #6 (Fig. 5).

To solve eqn. 3 for $r_T$ now only requires a value for $\hat{J}_{||}$ itself. If the thermoelectric effect were the sole driver of the observed current flow, then $J_{||c} + J_{||h} = 0$ on any given SOL flux surface (and note that $J_{||} = 0$ on the separatrix since $L_c \rightarrow \infty$). Since for the magnetic equilibrium studied here, the inner and outer probes do not correspond to the same flux surface, to check the constancy of $J_{||}$ from target to target requires interpolation amongst the probes. This has been performed for the ELM target current profile evolution discussed in the following section (see Fig. 21) and for the particular case of the location of probe #6, for which the $T_e$ has been calculated in Fig. 18, it appears that parallel current is indeed reasonably well balanced from target to target in the time interval around the ELM peak, although there is a consistent tendency for the magnitude of the inner currents to exceed those at the outer target, leading ultimately to a net total current favouring the inner target (see also below, Fig. 22).

Assuming therefore that the ratio $J^c_{||}/J^c_{sat}$ can be taken as a good approximation to $\hat{J}_{||}$, eqn. 3 can be solved numerically to yield the value of $r_T$ that would be compatible with the measured current subject to the uncertainties described above, notably in the parallel conductivity. The result is shown in Fig. 20 for the case of probe #6 in Fig. 18. It appears that the data would be roughly consistent with a time varying value of $r_T$ that reaches a peak of $r_T \sim 1.7$ at the peak of the ELM recycling emission. Since $J_{sat}$ at the inner target cannot be measured on this particular flux surface during the ELM as a consequence of the rapid fall in $V_f$, it is not possible to use this estimated temperature ratio to compute the expected power density at the inner target. But it would seem reasonable to assume that the higher $T_e$ predicted at the inner target would imply a higher power flux there. This is consistent with unpublished target heat flux data from ASDEX-Upgrade [40] in which, during experiments with SNL equilibria with unfavourable $B \times \nabla B$ direction (the analogue of this TCV case), Type I ELMs deposited more power to the inner target than the outer. The situation is reversed with normal direction of the toroidal magnetic field [17].

The calculation of temperature ratio represented in Fig. 20 is extremely approximative and

should be taken only as an indication that ratios of order 2 could explain the observed current flows as being thermoelectric in origin. As remarked earlier, however, some or all of the current could also be driven by parallel pressure imbalance, though it is impossible without additional data to deduce the relative importance of such effects. As to the origin of the $T_e$ asymmetry, Section 5 demonstrates that such ratios are commonly observed in TCV low density L-mode plasmas with similar magnetic equilibria and unfavourable BxVB drift direction. According to Fig. 20, $r_T \sim 1$ in the ELM-free period, but this cannot necessarily be interpreted with confidence since, as will be demonstrated below, the ELM-free parallel current balance at the particular location in the SOL appropriate to this calculation is not necessarily consistent with a thermoelectric origin. In contrast, during the ELM, it could well be the case that an in/out power asymmetry (ie. the ELM transports more power to the inner target) is simply responsible for the inferred asymmetry in $T_e$. Confirmation must await direct, fast measurements of the strike point $T_e$ which are in preparation at TCV.

### 4.4 Profiles of the ELM driven current and current balance

It is already clear from the raw data and the coherent averages (Figs. 7,13) that parallel current balance is not generally satisfied during these ELMs - there appears to be a surplus of current to the inner target. To investigate this more carefully and to see where such imbalance may originate in both time and spatial location, the coherently averaged $J_0$ in Fig. 13 can be mapped onto the target and then intepolated from target to target. Magnetic geometry is then eliminated and profiles of perpendicular target current, $J_{0\perp}$, can be compared at the usual place - the outside midplane.

The result is presented in Fig. 21 for a number of time slices during the coherent ELM. These times are indicated at the top of the figure on the coherent $D_\alpha$ trace. The split into two columns illustrates the profile evolution in the pre-ELM and ELM rise phase (left hand column) followed by the development at the ELM peak and beyond (right hand column). Blue shaded areas correspond to inner target currents and red to measurements at the outer target. A word of caution is appropriate with regard to the simple linear interpolation, which has been made from the outer target to the inner target in order to benefit from the higher effective spatial resolution on the inner target, itself a consequence of the increased flux expansion there (Fig. 5). Only those probes corresponding to field lines connecting from target to target around the main SOL (Fig. 5) have been included in this interpolation and so it is clear that comparatively few spatial

locations are thus transformed into approximately twice as many. (Note that the data from all inner probes in the connecting region - Fig. 5 - have been included in Fig. 21. This is a total of 12 data points in the inner divertor SOL compared with only 5 at the outer.) A further two probes in the private flux region have also been included in addition to the two private flux probes (#53,5) shown throughout in Figs. 4,6,7, 11-13. As usual, these profiles and the mapped midplane positions are averaged over the period 0.5-0.8 s during which the outer strike point position varies only slightly (see Section 3).

An immediately obvious feature of Fig. 21 is the large negative current spike that probably lies in the inner target private flux region. Although uncertainties in the equilibrium reconstruction are reasonably small at the strike points in view of the proximity of in-vessel poloidal field probes (Fig. 3) and certainly smaller than the inter-probe separation (~17 mm on the central column and 11 mm on the vessel floor), the location cannot be unambiguously determined. This narrow current feature is present in the ELM-free period before the ELM and returns after the ELM. Its magnitude dominates the inter-ELM current flow - a similar feature is not seen at the outer target, but this may be simply due to lack of spatial resolution there if the current is very localised. It would seem possible that this phenomena may be due to pressure driven flows and is also seen regularly in L-mode plasmas. Section 5 will have more to say on this issue.

In the pre- and post-ELM phases, the current in the main inner SOL can even be positive for positions not too far distant from the strike point. It is for this reason that the inter-ELM $T_e$ ratios computed from eqn. 3 in the preceeding section are almost certainly invalid - positive current of the same magnitude at both inner and outer strike points at the same location cannot be consistent with a thermoelectric origin.

As the ELM develops, the large negative inner private flux current spike is preserved at roughly its ELM-free value ($J_{0\perp} \sim 2$ Acm$^{-2}$), but now a larger negative current appears outside the separatrix in the common flux corresponding to the build-up of positive current at the outer target. Throughout the ELM $D_\alpha$ rise time and even at the ELM peak, the currents remain in reasonable balance at several locations in the SOL - these are the thermocurrents proposed in Section 4.3. Note that the rather smooth decrease of the outer target current profiles from their peak values towards the private flux region is artificial and a consequence of the simple interpolation - there are insufficient outer target probes in this region to determine how the profile shape decreases. Most of the ELM driven current flows in the first 5 mm of midplane

coordinate - likely the region most affected by an increase in SOL $T_e$ during the ELM.

After the ELM peak, the current appears to redistribute spatially at the inner target with the pre-ELM inner target positive currents reappearing near the inner strike zone. At the outer plate the profile simply relaxes montonically everywhere. Finally, several 100 μs post ELM, the situation is as before, with the inner private flux region negative current feature dominant.

Computation of global current balance is straightforward once the projected currents are available and toroidal symmetry of the ELM current is assumed (recall that the inner and outer probe arrays are located in separate toroidal locations). Figure 22 compiles the result of this integration, giving the coherently averaged total projected currents for inner and outer targets through the ELM, including, as before, all probes in the common flux and several in the private flux region. Indeed the effect of the narrow inner private flux negative current is evident on the integrated inner plate current which is characterised by a continuous offset of some 700 A throughout the ELM. In the lower panel of Fig. 22, this offset has been removed (as has that on the outer target integral current), by normalising to the values at t = -0.1 ms, corresponding approximately to the beginning of the $D_\alpha$ ELM rise. Inverting the negative inner target current integral also helps to compare both targets. It is clear that current balance is not perfectly satisfed during the ELM. Quantitatively, once the inter-ELM offsets have been removed, the difference for this example is almost exactly a factor 2 (2.17) in favour of the inner target.

Even accounting for the relative uncertainties resulting from the rather crude trapezoidal integration employed to derive these total currents and considering that an array of single Langmuir probes cannot hope to approach the accuracy of a direct measurement of the currents using tile shunts, the in/out asymmetry evident in Fig. 22 must be partly due to a real effect. No unambiguous candidate is offered here, but it is possible that increased plasma interaction with the chamber walls during the ELM might be responsible for the extra current - the return path of the current is likely distributed over a larger surface area, perhaps at the central column. It is known that the ELM burst can be detected on sensors (eg. Langmuir probes, visible light emission) located at or near the walls, often with large amplitude [25]. As was already remarked in Section 2.4, this is indeed also the case in TCV, as illustrated in Fig. 8 by the $J_{sat}$ trace on Pin 5 of the fast reciprocating probe. At a separatrix distance of ~20 mm, corresponding to the outer wall radius at the midplane, ion saturation current spikes of 20 $Acm^{-2}$ are still visible.

It worth noting that the total integrated currents in Fig. 22 are not trivial in magnitude. Ignoring the factor 2 discrepancy and taking the outer target current as a lower bound on the

parallel ELM driven current, its peak value represents ~0.5% of the plasma current flowing in the same direction as the latter.

Target ELM currents have been observed previously at JET [41], but the reported data are for giant (Type I) ELMs driving currents of order 100 $Acm^{-2}$ near the strike points. No profile information such as that described here was available, but crude estimates based on toroidal symmetry and a fully parallel current yielded total target currents of order 150 kA, corresponding to ~5% of $I_p$. Interestingly, the ELM current was observed to be positive (from plasma to target) at both strike points (with a large radially inwards displacement of the inner target current during the ELM). This is suggestive of a fundamental difference between the smaller (probably Type III) TCV ELMs and larger events (Type I). Whilst the smaller ELMs can apparently drive currents by provoking $T_e$ asymmetries, larger perturbations may actually be depositing part of the plasma current into the SOL [42]. Even if this is not the case, the larger events are probably of sufficient magnitude that "burn-through" of the divertor plasma occurs readily at both targets, providing instantaneous temperature symmetrisation of the target plasmas, perhaps preventing the flow of thermoelectric currents. More measurements of the kind reported here would therefore be of great interest, particularly across transitions from one ELM type to another and for both directions of toroidal field (in which in/out divertor target asymmetries are likely to differ)

## 5. L-MODE TARGET CURRENTS IN TCV

To close this paper, it is appropriate to compare and contrast the more complex ELM situation with the somewhat more quiescent ohmic L-mode case. To do so, a similar magnetic equilibrium is chosen (see inset of Fig. 24) at a somewhat lower plasma density and current ($I_p$ = 340 kA) to the ELMing H-mode cases that have been discussed in the preceeding sections. The outer target flux expansion is also higher in this L-mode example, though this is a minor detail and does not change the principle observations save for providing higher spatial resolution at the outer plate. In common with the H-mode discharges, the $B \times \nabla B$ drift is directed upwards, away from the X-point.

A selection of results extracted from analysis of swept probe characteristics is compiled in Fig. 23 for probes #5 and #52, computed to be those nearest the outer and inner strike points respectively in the common flux region for much of the discharge. Note, however, that flux mapping and interpolation have not been performed here so that these two probes do not quite

correspond to the same flux surface - the inner target probe #52 is marginally closer to the strike point than probe #5, though the difference is too small to be of much importance. In common with the H-mode discharges, however, the outer strike point does move naturally radially inwards during the latter part of the discharge.

This L-mode example shows clearly that at low densities there is a natural $T_e$ asymmetry which, in combination with similar local electron densities, leads to an apparent electron pressure ($P_e$) asymmetry, at least close to the strike points even under attached conditions. Some of the asymmetry may, however, be explained by uncertainties in the determination of $T_e$ with the use of target Langmuir probes [39].

Figure 23 also illustrates the time traces of $J_{0\perp}$ obtained by extracting the current at V = 0 from the probe characeteristics and not by holding the probe at constant zero bias as required during the ELMing discharges. For both inner and outer targets, data from probes either side of the strike point probe are included (green traces on the private flux side, magenta on the SOL side and black for the two probes #5, 52). The narrow feature of strong negative current is evident in the inner private flux region (green trace) as it was for the coherently averaged ELM current. At the outer target, there is now also evidence for a negative current spike in the private flux, though of much lower amplitude. As the discharge progresses and the outer strike point position moves gradually inwards, this feature becomes suddenly more prominent (around 0.7 s), though still of reduced amplitude compared with the inner target. This sudden increase of current and the subsequent decrease as the outer leg moves steadily further inward and away from the probe indicates that also here the feature is rather localised.

Total current balance for inner and outer targets is given in the lower panel of Fig. 23, where only contributions from the common flux have been summed to avoid the large offset due to the inner target negative current spike (for comparison with the lower panel of Fig. 22 for the coherent ELM current balance). Unlike the ELM driven current, parallel balance is closely satisfied in this ohmic L-mode throughout the discharge, lending some support to the belief that increased wall interaction during the ELM, absent in the L-mode, might be responsible for the inner target excess. One should also note that the ELM driven total current exceeds this natural L-mode value by as much as a factor 4.

In analogy to Fig. 21 for the ELM current profile, Fig. 24 plots the the spatial distribution of $J_{0\perp}$ in midplane coordinates for inner and outer targets. As for the H-mode cases, only data in the interval before the outer strike point position has moved appreciably (in this particular

example the period 0.5 - 0.7 s) is included. Note the increased outer target spatial resolution due to the increased flux expansion there in comparison with the H-mode discharges of earlier sections. The profiles are very reminiscent of those found before and after the coherent ELM in Fig. 21 (top left and bottom right panels) and are extremely similar to those reported by Schaffer et al. [43] in the JET tokamak during L-mode discharges operated with reversed $B_\varphi$ ($B \times \nabla B$ drift direction away from the X-point in SNL). In JET too, the negative current feature (for positive $B_\varphi$) in the private region was stronger at the inner target than at the outer. In addition, the JET data also show a tendency for the inner target current profile to exhibit a region of positive current near the separatrix before reversing deeper in the SOL to form a broad shoulder of negative current. The TCV equilibrium reconstruction places the inner target narrow current feature marginally in the SOL, but the probe separation of 17 mm together with the absence of strike point sweeping makes unambiguous localisation impossible.

These narrow current density peaks near the strike points or just inside the private flux region are almost certainly parallel currents (referred to as Pfirsch-Schlüter currents in [43]) arising from the divergence of the surface averaged radial current driven by the combined effect of the ion $B \times \nabla B$ drift and the up/down asymmetry of plasma pressure [44]. They are of the correct sign (negative) for reversed $B_\varphi$ and should reverse (become positive) in the common flux region of the SOL at both targets. These currents may also explain the tendency for a positive current in part of the inner divertor SOL where the Pfirsch-Schlüter and thermoelectric currents compete. The latter are in addition due to a combination of target temperature and pressure asymmetries. It is not the purpose of this contribution to present a detailed analysis of these current flows, nor does the quality of the data make this an easy task. Instead, this brief comparison with L-mode data serves to demonstrate simply that ELM-free periods appear similar to L-mode in the form of target current profile. During the ELM perturbation itself, there is strong evidence that in TCV, at least for the particular type of ELM studied here, the thermoelectric current driven, most likely by temperature asymmetries provoked by the ELM, is responsible for a considerable increase in the magnitude of the parallel current.

## 6. SUMMARY AND CONCLUDING REMARKS

Providing sufficiently uniform ELMing phases can be produced in repeated, similar discharges, the combination of moderately fast data acquisition and good spatial resolution of single Langmuir probes operating in fixed bias modes together with simple coherent averaging

is a demonstrably useful technique for study of ELM interactions with the divertor target. Observations in SNL plasmas with unfavourable ion BxVB drift direction on TCV have revealed the presence of rather strong parallel (to the total magnetic field) currents flowing in the SOL during ELMs superimposed on a natural flow pattern which appears to be similar in both L-mode and ELM-free H-mode phases.

The direction of these ELM generated currents would be consistent with a thermoelectric origin if the inner target is preferentially heated by the ELM energy pulse in comparison with the outer target. In TCV, for the SNL equilibrium studied in this paper with positive $I_p$ and $B_\varphi$, the total integrated currents approach ~0.5% of the plasma current and flow in the same direction as $I_p$. They are significantly lower than and flow in a different direction to the very large currents that have been measured during large ELMs on JET (up to 5% of $I_p$), indicating that very large perturbations drive currents through different mechanisms. Quite apart from their physics interest, these ELM driven currents have recently been suggested [45] as a route to mitigating the potentially intolerable energies deposited on the targets by the ELM through the natural strike point sweep that would be generated by radial ExB drifts provoked when toroidally adjacent flux tubes are made to intersect target tiles with appropriately chosen varying resistance paths to machine earth.

In addition to revealing the nature of target current flows during the ELM, the coherently averaged single Langmuir probe ELMs can, under some circumstances, also provide estimates of the target plate parameters ($T_e$, $n_e$ and power flux), even if these are not directly accessible when operating the probes in the fixed biased modes required for sufficient time resolution during the ELM. Results from TCV for the time evolution of $T_e$ near the strike point during the ELM are in good agreement, both in absolute magnitude and temporal response with those reported from JET obtained with the use of triple Langmuir probes yielding $T_e$ directly with high time resolution.

It is probably only by some kind of averaging that detailed comparisons of the evolution of experimentally measured target parameters such as local floating potential, current and $T_e$ can be compared with the predictions of kinetic models, which are now reaching a level of maturity permitting such comparisons and are being improved to provide a more realistic model of the complex interactions with recycling neutrals and impurities characteristic of the divertor target region. Indeed, the TCV data are in qualitative agreement with the expectations of 1D particle-in-cell modelling of the transport of ELM energy down the SOL. In particular, the basic premise

that the ELM energy pulse at the target consists of an initial burst of fast electrons released from a region upstream localised near the outside midplane, followed by an ion heat pulse carrying most of the ELM energy and arriving on the timescale of the ion transit time down the SOL to the target, is not inconsistent with the experimental findings reported here. For TCV at least, the probe data also provide (through the observed temporal modifications to the probe floating potential) strong evidence that these fast electrons are released already very early on in the development of the coherent magnetic precursor phase observed near the outside midplane.

Unfortunately, insufficient experimental information exists on TCV at the time of writing to unambiguously identify the ELM type discussed in this paper. There is a good deal of evidence for a Type III classification, but it is not the purpose of this contribution to address this issue. Instead, the results presented here are hopefully suggestive that similar observations might be worthwhile in other devices with a wider range of ELM types than TCV can presently access. Experiments should also be performed, if possible, for both directions of toroidal field in order to assess the influence of divertor asymmetries in determining the parallel currents pre-ELM and indeed the consequence, if any, of the field direction on the ELM power deposition asymmetry and hence on the current flow.

ACKNOWLEDGEMENTS

Helpful discussions with A. V. Chankin and A. Loarte are gratefully acknowledged. Thanks are also due to Y. R. Martin for finding a way to produce the stable ELMing ohmic H-mode plasmas descrbed here and to J.-M. Moret for analysis of the diamagnetic loop data. This work was partly funded by the Swiss National Foundation for Scientific Research.

## REFERENCES

[1] Loarte, A., et al., Plasma Phys. Control. Fusion **44** (2002) 1815.

[2] Becoulet, M., et al., Plasma Phys. Control. Fusion **44** (2002) A103.

[3] Zohm, H., Plasma Phys. Control. Fusion **38** (1996) 1213.

[4] Suttrop, W., Plasma Phys. Control. Fusion **42** (2000) A1.

[5] Chankin, A. V., et al., Nucl. Fusion **42** (2002) 733.

[6] Leonard, A., et al., Plasma Phys. Control. Fusion **44** (2002) 945.

[7] Connor J. W., Plasma Phys. Control. Fusion **40** (1998) 531.

[8] ITER Physics Basis, Nucl. Fusion **39** (1999) 2137.

[9] Bergmann, A., Nucl. Fusion **42** (2002) 1162.

[10] Weisen, H., et al., Plasma Phys. Control. Fusion **38** (1996) 1137.

[11] Martin, Y. R., et al., 18th IAEA Fusion Energy Conf., Sorrento, Italy, 4-10 October 2000, IAEA-CN-77/EXP5-30

[12] Hogge, J.-P., et al., submitted to Nucl. Fusion

[13] Pitts, R. A., et al., Nucl. Fusion **39** (1999) 1433.

[14] Pitts, R. A., et al., J. Nucl. Mater. **290-293** (2001) 940.

[15] Reimerdes, H., et al., Nucl. Fusion **38** (1998) 319.

[16] Porte, L., et al., 19th IAEA Fusion Energy Conf., Lyon, France, 14-19 October 2002, IAEA-CN-94/EXP5/15

[17] Herrmann, A., et al., Plasma Phys. Control. Fusion **37** (1995) 17.

[18] Boedo, J. A., et al., Rev. Sci. Intrum. **69** (1998) 2663.

[19] Rudakov, D. L., et al., Plasma Phys. Control. Fusion **44** (2002) 717.

[20] Moret, J.-M., et al., Rev. Sci. Intrum. **69** (1998) 2333.

[21] Reimerdes, H., Phd thesis, CRPP-EPFL report LRP 700/01 (2001).

[22] Blanchard, P., et al., Plasma Phys. Control. Fusion **44** (2002) 2231.

[23] Stangeby, P. C., "The Plasma Boundary of Magnetic Fusion Devices", Bristol, Institue of Physics Publishing, (2000).

[24] Petrie, T. W., et al., J. Nucl. Mater., in press.

[25] Counsell, G. F., et al., Plasma Phys. Control. Fusion **44** (2002) 827.

[26] Krasheninnikov, S., Phys. Lett. A **283** (2001) 368.

[27] Stangeby, P. C., Plasma Phys. Control. Fusion **37**(1995) 1031.

[28] Jachmich, S., et al., Proc. 28th EPS Conf. on Control. Fusion and Plasma Phys., Funchal, 18-22 June 2001, ECA **25A** (2001) 1617.

[29] Laux, M., et al., Proc. 28th EPS Conf. on Control. Fusion and Plasma Phys., Funchal, 18-22 June 2001, ECA **25A** (2001) 1625.

[30] Herrmann, A., et al., J. Nucl. Mater., in press.

[31] Tskhakaya, D., et al., 9th EU-US Transport Task Force Workshop, Cordoba, Spain, 9-12 September 2002, paper O.I.03

[32] Staebler, G. M., Hinton, F. L., Nucl. Fusion **29** (1989) 1820.

[33] Stangeby, P. C., Nucl. Fusion **30** (1990) 1153.

[34] Harbour, P. J., Contrib. Plasma Phys. **28** (1988) 415.

[35] Harbour, P. J., et al., J. Nucl. Mater. **162-164** (1989) 236.

[36] Chankin, A. V., et al., J. Nucl. Mater. **196-198** (1992) 739.

[37] Schaffer, M. J., Leikind, B. J., Nucl. Fusion **31** (1991) 1750.

[38] Kumagai, A., et al., Plasma Phys. Control. Fusion **39** (1997) 1189.

[39] Horacek, J., et al., J. Nucl. Mater., in press.

[40] Herrmann, A., Eich, T., private communication.

[41] Lingertat, J. V., et al., J. Nucl. Mater. **241-243** (1997) 402.

[42] Solano, E. R., et al., IEA Workshop on ELMs (IEA Large Tokamak Collaboration), JET Facility, Culham Science Centre, Abingdon, OXON OX14 3DB, UK, 24-26 June 2002.

[43] Schaffer, M. J., et al., Nucl. Fusion **37** (1997) 1750.

[44] Chankin, A. V., J. Nucl. Mater. **241-243** (1997) 199.

[45] Stangeby, P. C., submitted to Nucl. Fusion.

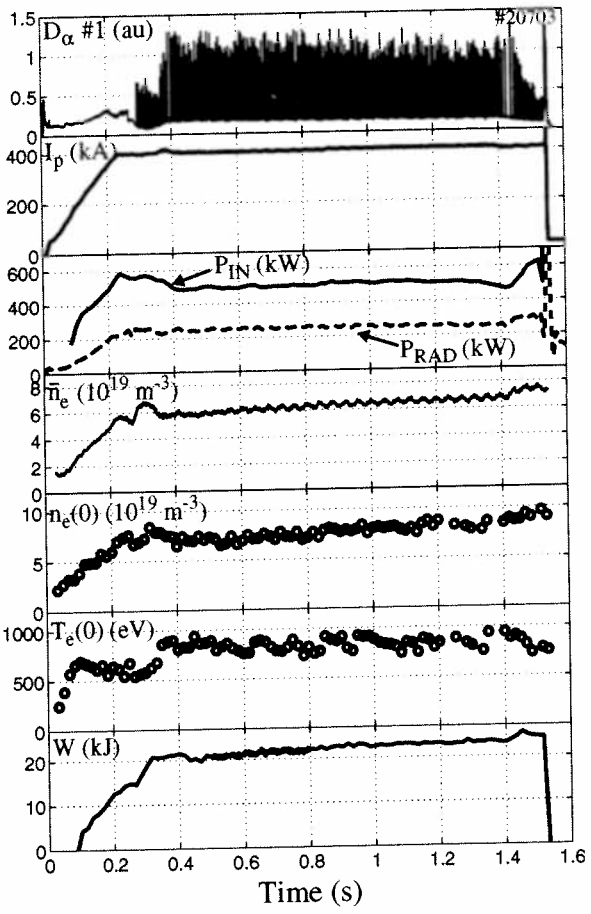


Fig. 1. Relevant plasma signals for a typical ELMing H-mode (#20703) in the TCV tokamak and from which some of the the scrape-off layer data reported here have been obtained. The magnetic equilibrium is shown in Fig. 3 and is a SNL configuration with the high field side (HFS) divertor leg on the central column and the low field side (LFS) strike point on the vessel floor. The L-H transition occurs at 267 ms, when $I_p$ and all plasma shape parameters have reached their plateau values. The $D_\alpha$ emission is measured using the vertical line of sight sketched in Fig. 3. $T_e(0)$, $n_e(0)$ are measured using Thomson scattering and stored energy, W, is obtained from the equilibrium reconstruction.

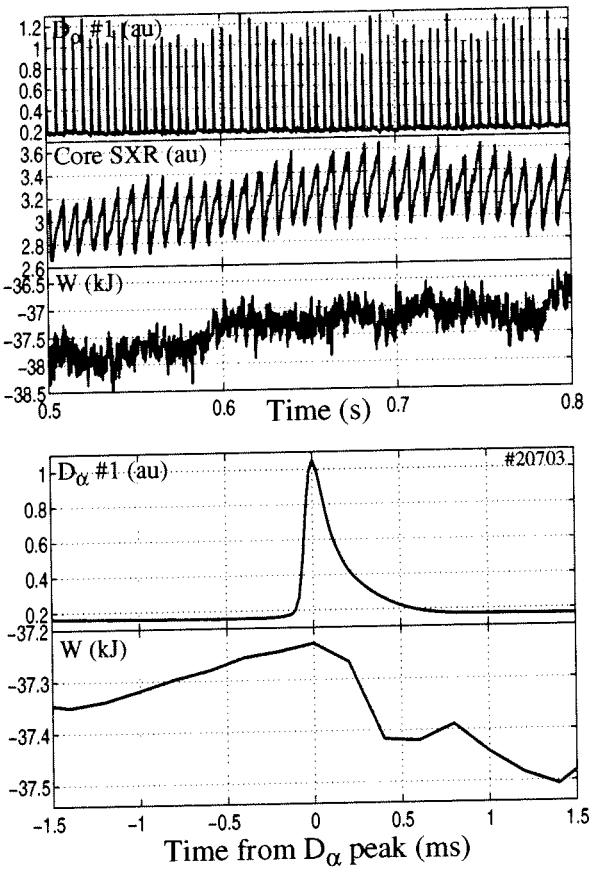


Fig. 2. The period t = 0.5-0.8 s in the discharge of Fig. 1 is used throughout this paper when coherently averaging various plasma signals. Here, the process has been performed for the diamagnetic loop data (W) which are on the limit of signal to noise for these 200 Hz ELMs (top $D_\alpha$ trace). The soft X-ray (SXR) diode signal from a line of sight viewing the plasma core illustrates the lower sawtooth frequency. The coherently averaged DML signal (with a timebase of t = 0 at the peak of the coherently averaged $D_\alpha$ ELM) indicates an average energy loss per ELM of ~ 300 J.

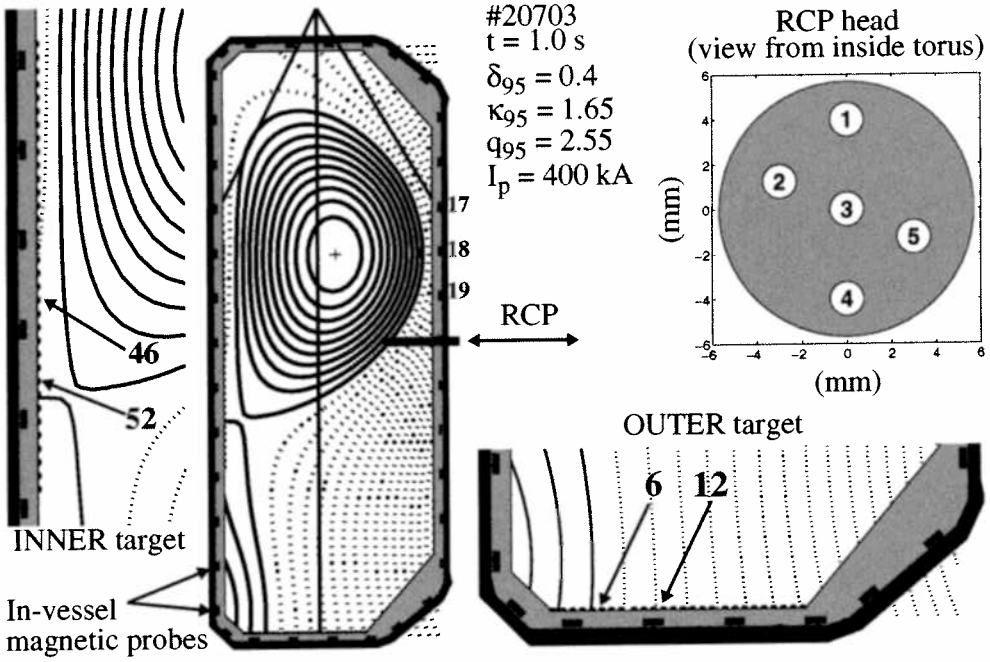


Fig. 3. Indicating the positions of the fixed divertor target Langmuir probes, the fast reciprocating Langmuir probe and the TCV magnetic equilibrium used to obtain the data reported here. Representative probe numbers are indicated in the expanded divertor views for later reference. Probe numbers 1-26 lie on the vesel floor, numbers 27-60 on the central column. A 5 pin, fast reciprocating Langmuir probe enters the machine at the vessel midplane. The line of sight and approximate acceptance angle of the main $D_\alpha$ emission detector are superimposed on the equilibrium. The in-vessel poloidal magnetic field probe positions of one complete poloidal array are also marked, with particular emphasis on the outer midplane probes 17-19, data from which will be used in Section 2.4.

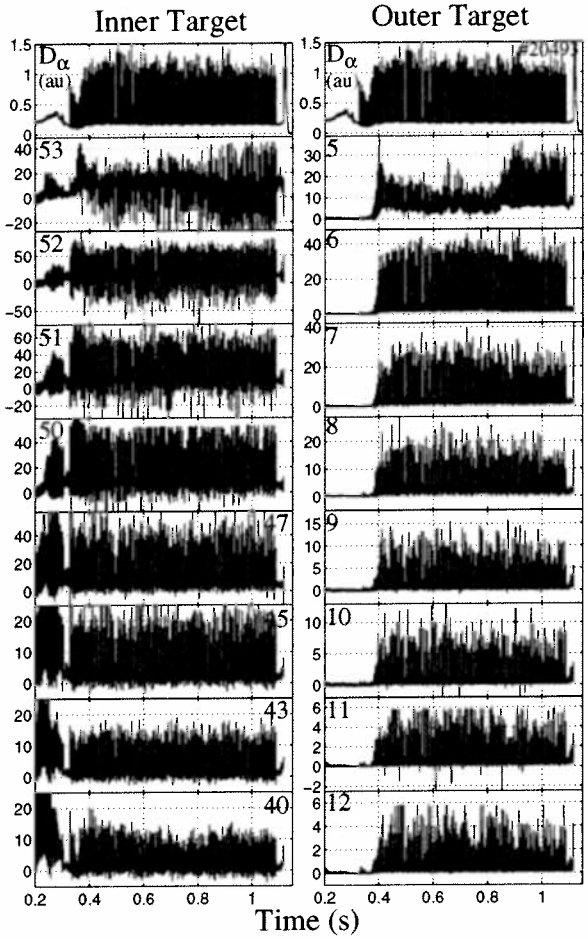


Fig. 4. Time response of parallel ion saturation current densities, $J_{sat}$ (in $Acm^{-2}$) to inner (left) and outer (right) target probes during ELMs. For each target the probe positions are progressively further away from the strike point in moving down each column (see Fig. 3). Probes 52 (inner) and 6 (outer) are closest to the strike points in the SOL. At the top of each column for comparison is the $D_\alpha$ emission along a vertical chord through the plasma. Discharge parameters and magnetic equilibrium are identical to those of Fig. 1.

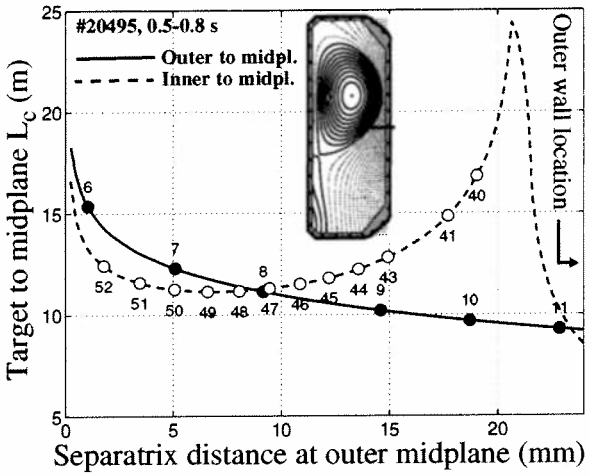


Fig. 5. Connection lengths along the total magnetic field from outer and inner divertor targets to the outer midplane as a function of distance from the separatrix. (values averaged over the period 0.5-0.8 s). Probes from which data are shown in Figs. 3,5,6 are marked (outer target, full circles, inner target, open circles). Probes 53 (inner) and 5 (outer) are in the private flux region and are not shown. The field line from Probe 12 at the outer target connects to the outer wall before reaching the outside midplane. At the separatrix, the fast probe poloidal location is some 4 m downstream of the outer midplane in terms of parallel connection length

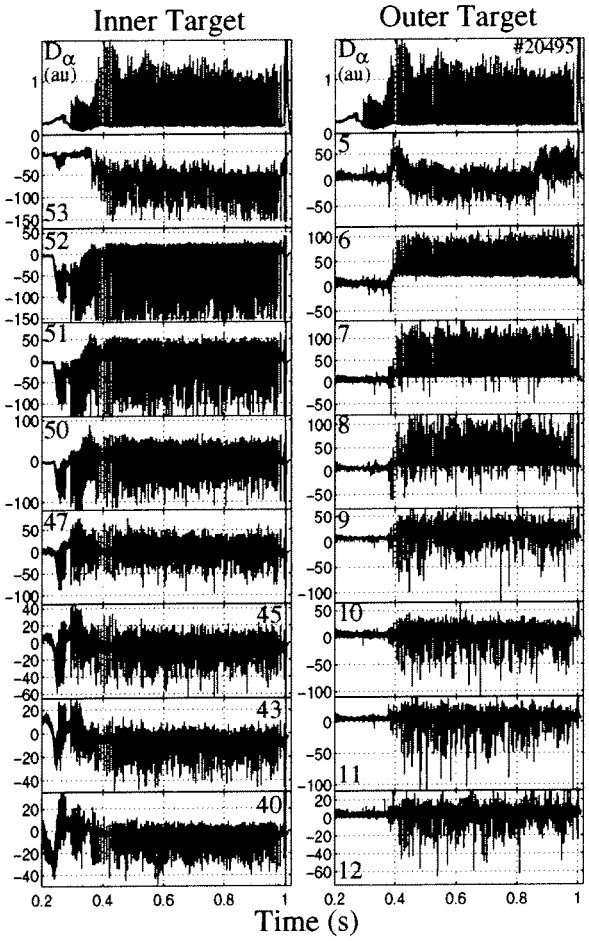


Fig. 6. Equivalent of Fig. 4 for the time dependence during ELMs of the floating potentials, $V_f$ (in Volts) to inner (left) and outer (right) target probes. Discharge parameters and magnetic equilibrium are identical to those of Fig. 1.

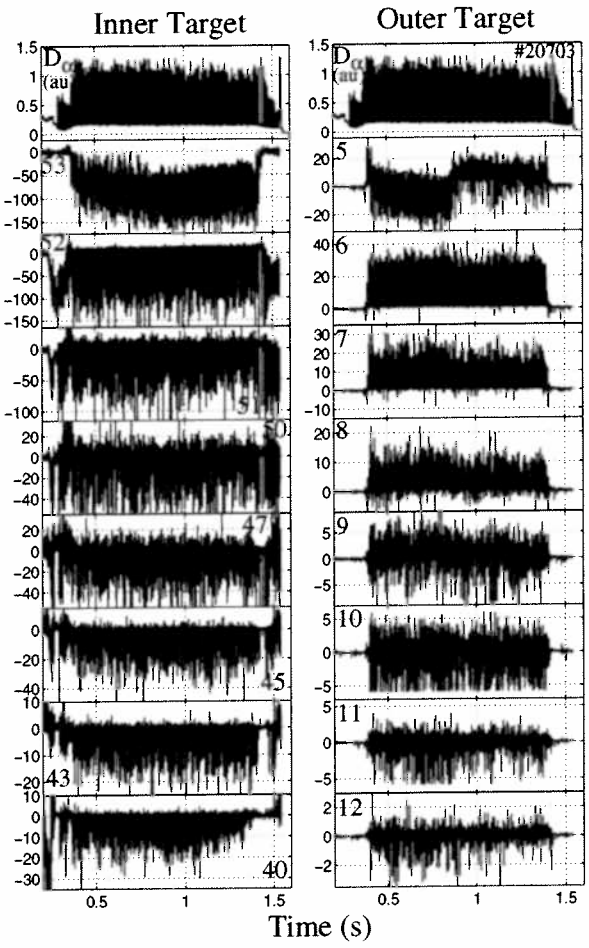


Fig. 7. Equivalent of Figs. 4,6 but illustrating the time dependence during ELMs of probe current densities $J_0$, (in $Acm^{-2}$) for probe bias voltage, V = 0, to inner (left) and outer (right) target probes. Refer to Fig. 1 for the evolution of plasma signals in this discharge and Fig. 3 for the magnetic equilibrium.

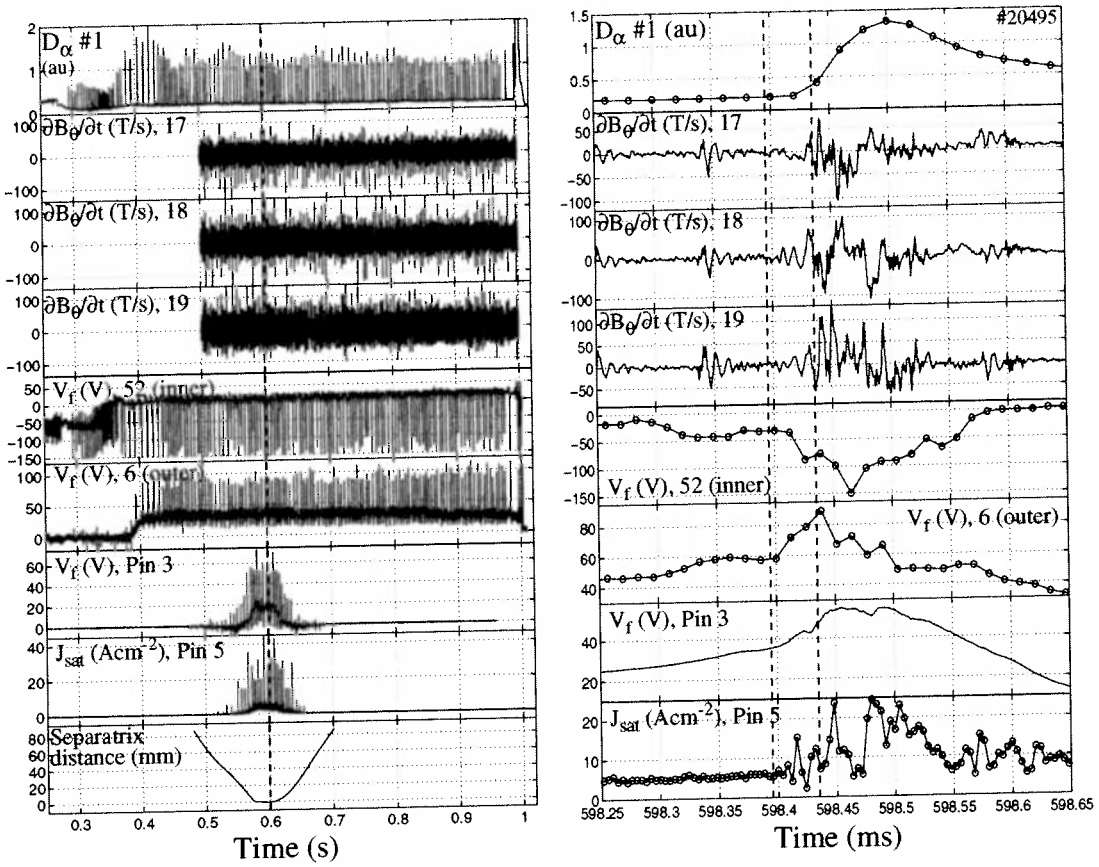


Fig. 8. On the left illustrating the time dependence of magnetic probe signals from in-vessel poloidal field probes near the outer midplane of the equilibrium (see Fig. 3) for the ELMing H-mode discharge #20495 (from which the data in Fig. 4 are obtained), $V_f$ for the probes at the inner and outer strike points closest to the separatrix (repeated from Fig. 6) and $V_f$ and $J_{sat}$ from two selected RCP pins (see Fig. 3). The envelope of the probe movement with respect to the separatrix at the probe poloidal location is given at lower left. On the right, an expanded area of the time around the dashed vertical line in the left hand figure near 0.6 s, concentrating on just a single ELM. The two vertical dashed lines in the right figure delimit the time over which the poloidal magnetic field probes see a coherent precursor.

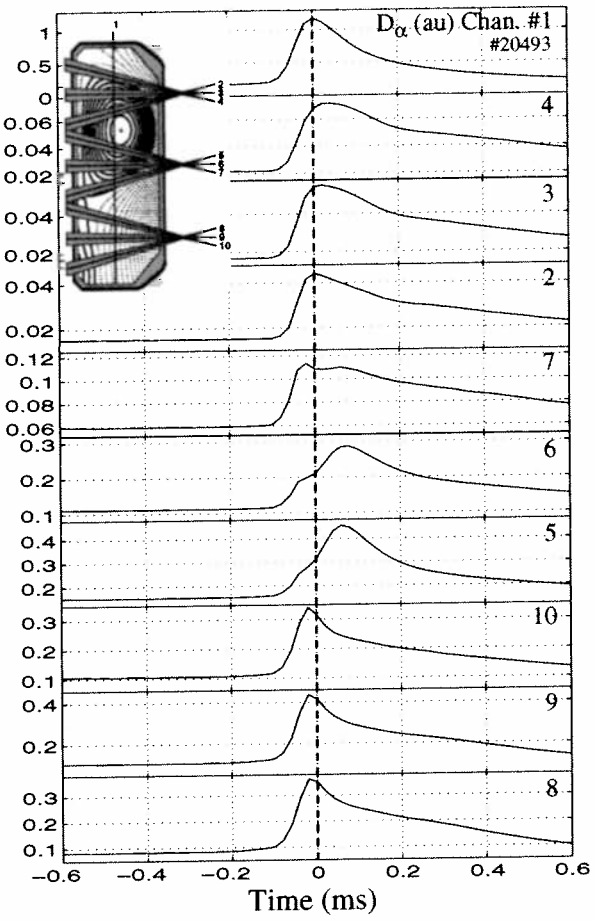


Fig. 9. Coherent averages over the interval 0.5-0.8 s of the $D_\alpha$ recycling emission along line integrals across the TCV poloidal cross-section in shot #20493. The channel disposition and approximate angular fields of view for the lateral channels are given in the inset. Channel 1 is the vertical LOS used for reference throughout this paper (Fig. 3) and has an unapertured field of view giving a much larger signal intensity than for the lateral channels (Nos. 2-10) whose intensities are multiplied by 10 here for clarity.

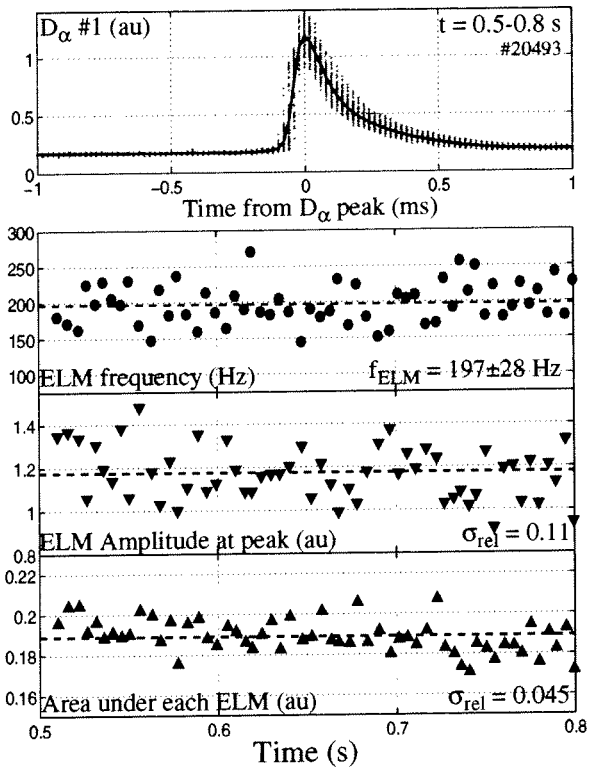


Fig. 10. At the top, the coherently averaged $D_\alpha$ ELM over the period 0.5-0.8 s superimposed on points from all ELMs in the interval. The lower traces illustrate the relatively low scatter in ELM frequency, amplitude and area enclosed by each ELM ($\sigma_{rel}$ is the relative error about the mean value, marked by the horizontal dashed lines in each trace).

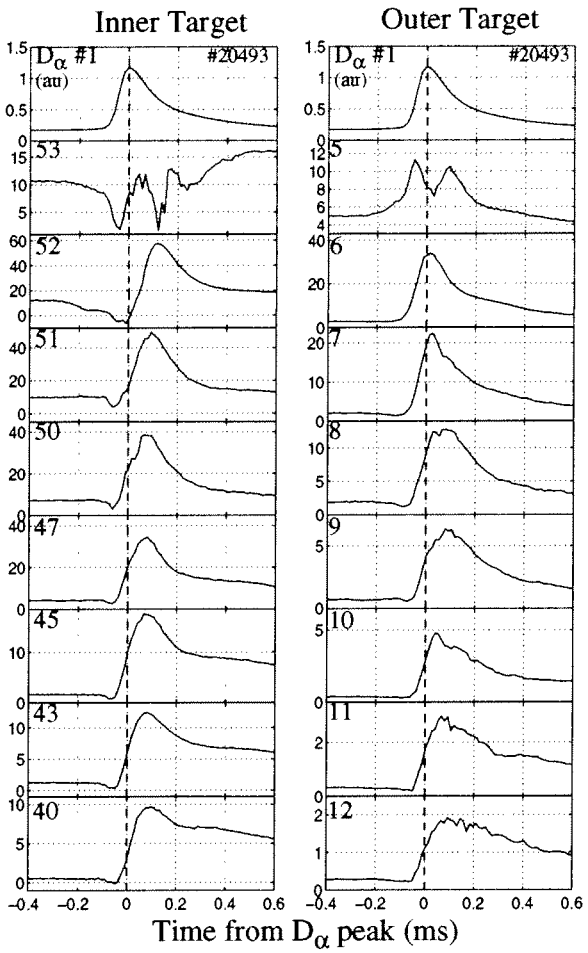


Fig. 11. Coherently averaged ion saturation current densities (in $Acm^{-2}$ measured at -100 V) to inner (left) and outer (right) target probes during the period 0.5-0.8 s in Fig. 4. The peak of the coherently averaged $D_\alpha$ vertical LOS signal (top trace) is used as the zero time reference for the probe signals - the vertical dot-dashed lines at t = 0 mark this reference point.

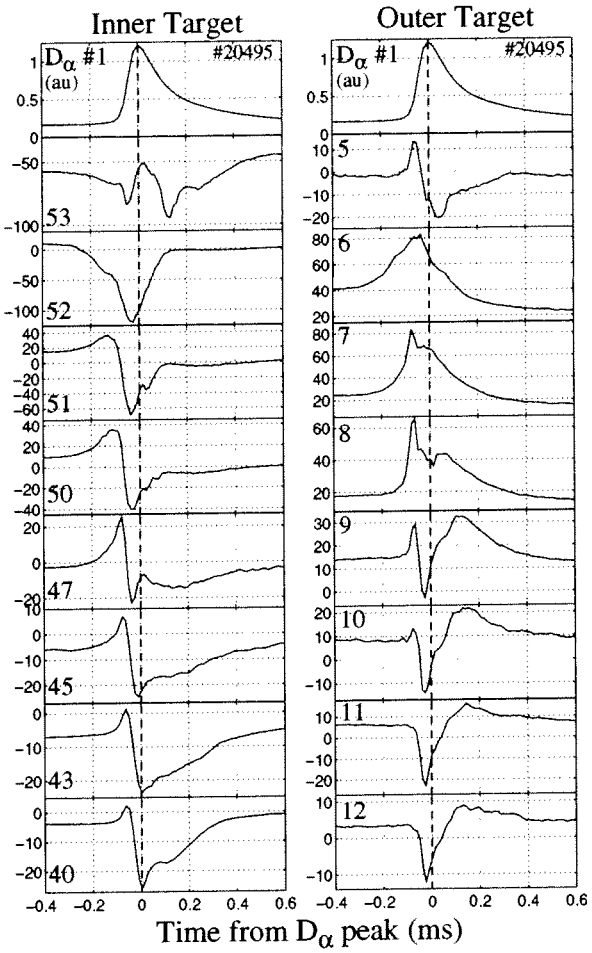


Fig. 12. Equivalent of Fig. 11 for the coherently averaged time dependence of floating potentials (in Volts) to inner (left) and outer (right) target probes during the period 0.5-0.8 s in Fig.6. The peak of the coherently averaged $D_\alpha$ vertical LOS signal (top trace) is used as the zero time reference for the probe signals.

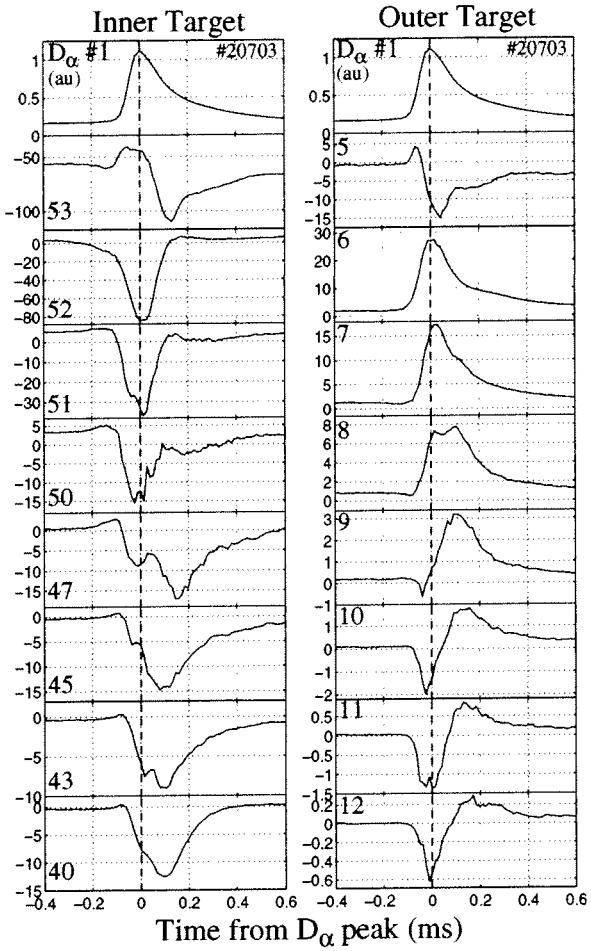


Fig. 13. Equivalent of Figs. 11, 12 for the coherently averaged time dependence of currents at zero volts (in $Acm^{-2}$) to inner (left) and outer (right) target probes during the period 0.5-0.8 s in Fig. 7. The peak of the coherently averaged $D_\alpha$ vertical LOS signal (top trace) is used as the zero time reference for the probe signals.

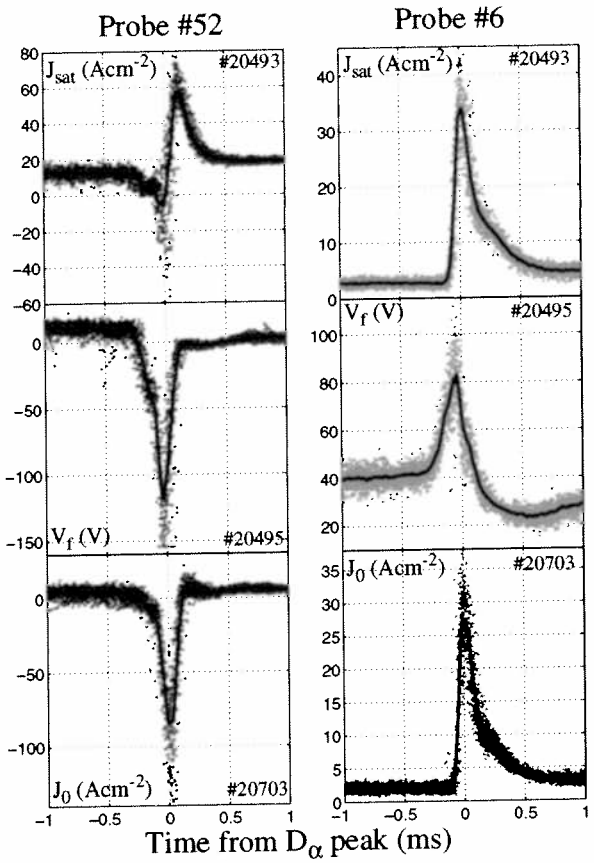


Fig. 14. Comparison of coherently averaged ELMs (solid lines) in $J_{sat}$, $V_f$ and $J_0$ with all individual ELMs in the period 0.5-0.8 s for the inner strike point probe #52 (blue) and probe #6 (red) closest to the outer strike point. Recall that the data are obtained from three separate, but very similar discharges.

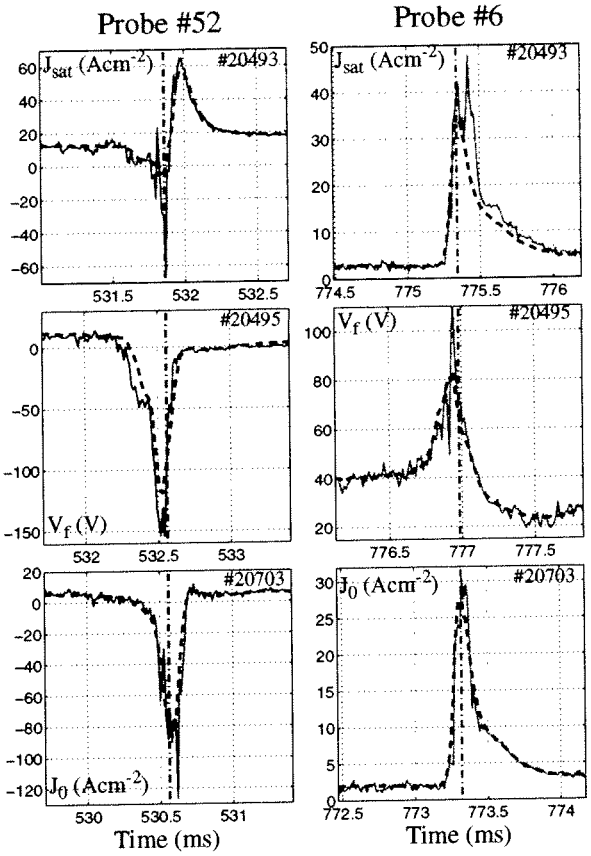


Fig. 15. Analog of Fig. 14 for selected individual ELMs (solid lines) compared with the coherent averages (dashed lines) for the three quantities, $J_{sat}$, $V_f$ and $J_0$ from the inner and outer strike point probes #52 (blue) and #6 (red) respectively. Whilst the coherent average is a reasonable representation of the target probe ELM, strong and rapid fluctuations are often present in the probe data, typically near the peak of the ELM perturbation on $D_\alpha$, marked by the vertical dot-dashed line in each case.

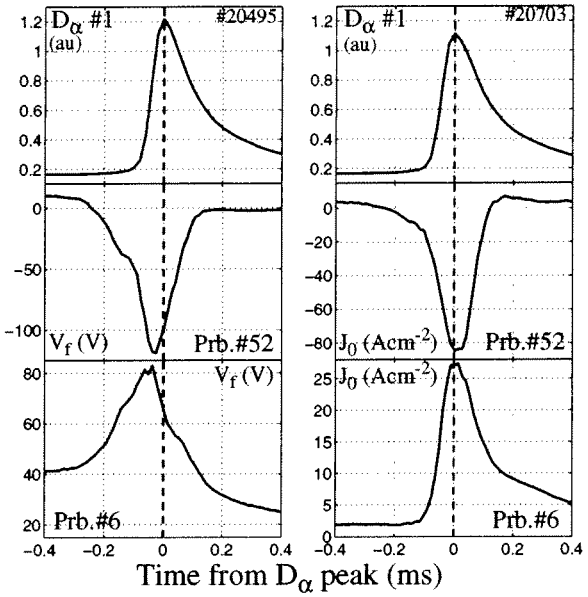


Fig. 16. Coherent ELMs in $V_f$ (left) and $J_0$ (right) in the period t = 0.5-0.8 s for the two probes (#52 and #6) nearest the inner and outer strike points together with the coherent $D_\alpha$ ELM appropriate to each discharge. The $V_f$ signals show a clear reaction long before any significant recycling emission due to the ELM is apparent. Similar behaviour is also observed on the inner target $J_0$, but not on the outer target current.

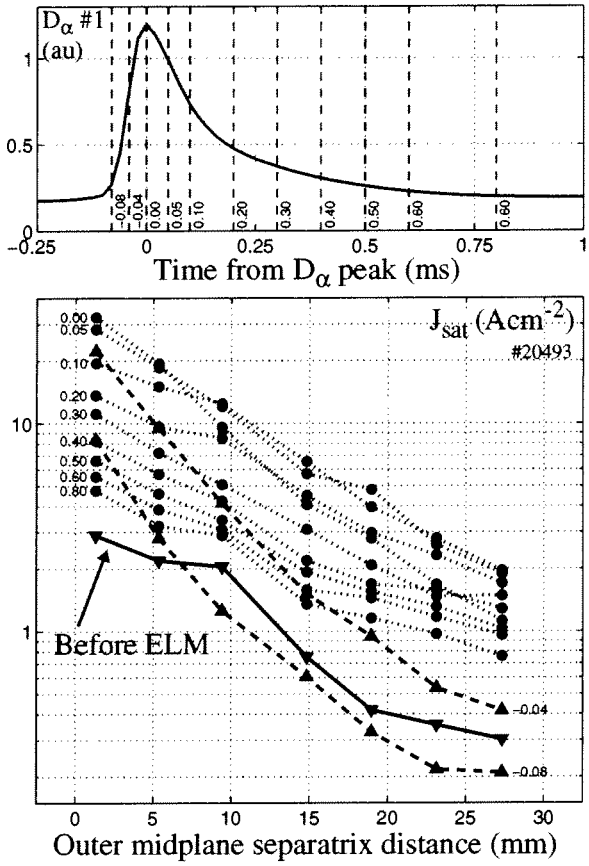


Fig. 17. Profiles of outer target $J_{sat}$ obtained using the coherent ELM averaged over the period 0.5-0.8 s (the computed midplane separatrix distances are also averaged over the same period). Similar profiles at the inner target cannot be produced owing to the strong negative dip in $V_f$ there, preventing ion saturation from being reached. Each profile corresponds to a single time in the $D_\alpha$ ELM, marked in the top trace by the vertical dashed lines. The two dashed line profiles are in the $D_\alpha$ rise phase, the dotted profiles from t = 0 and beyond. Each full symbol on each profile corresponds to a probe location on the outer target. Only probes in the common flux region are included.

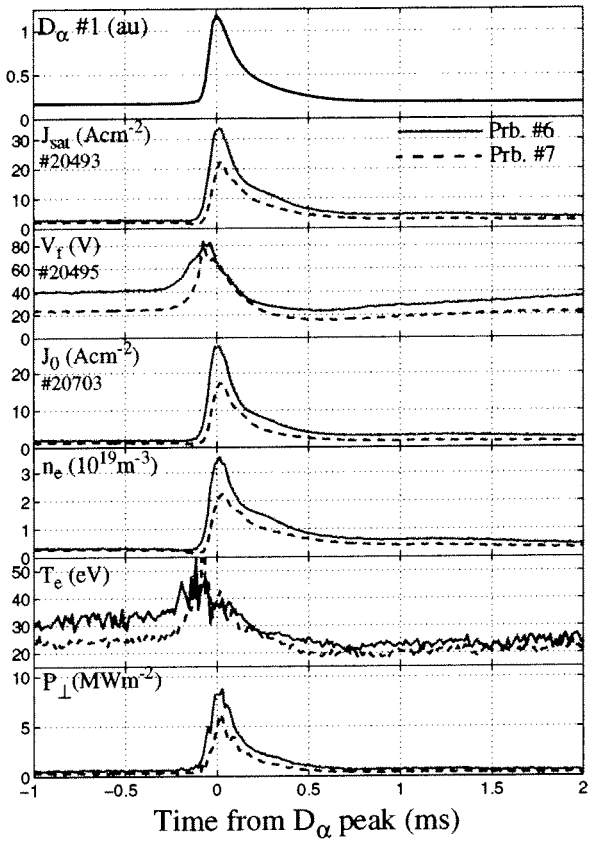


Fig. 18. Estimated $n_e$, $T_e$ and perpendicular power flux density near the outer target strike point computed using the coherent ELMs (averaged over the period 0.5-0.8 s) for $J_{sat}$, $V_f$ and $J_0$ together with the standard expression for the magnetised Langmuir probe characteristic (eqn. 2). Data for the two probes 6 (red full lines), 7 (blue dashed lines), nearest the outer strike point in the common flux region are shown. Note that the derived parameters are obtained by combining coherent signals from separate, similar discharges.

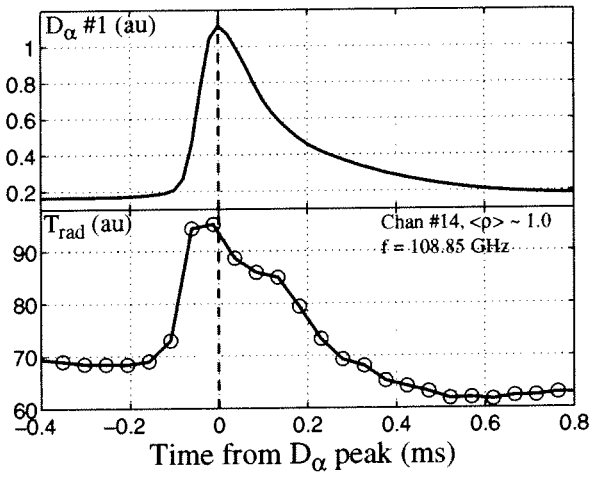


Fig. 19. Coherently averaged LFS ECE radiometer signal over the period 0.5-0.8 s for a channel with resonance frequency corresponding to a vertical line essentially coincident with the HFS separatrix of the SNL equilibrium (Fig. 3). The absolute magnitude of the signal cannot be simply interpreted as an electron temperature, nor is the acquisition frequency ideal, but there is evidence for an earlier perturbation with respect to the $D_\alpha$ emission.

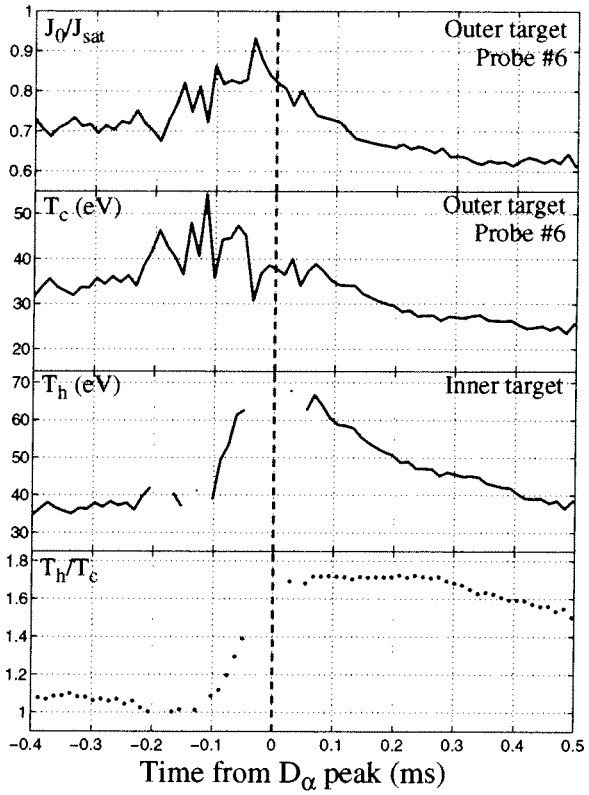


Fig. 20. Coherent average of the estimated $T_e$ ratio (eqn. 3) between inner and outer targets at the location of outer target probe #6 based on the ELM driven currents being of thermoelectric origin (assuming no target to target pressure imbalance). $T_c$ is the $T_e$ from Fig. 19, $T_h$ the result of multiplying $T_c$ by the computed ratio in the lower panel. If the ELM driven current is entirely thermoelectric and due only to an in/out $T_e$ asymmetry, the data imply a maximum ratio ~ 1.7 at the ELM peak, implying that the ELM delivers higher power flux to the inner target

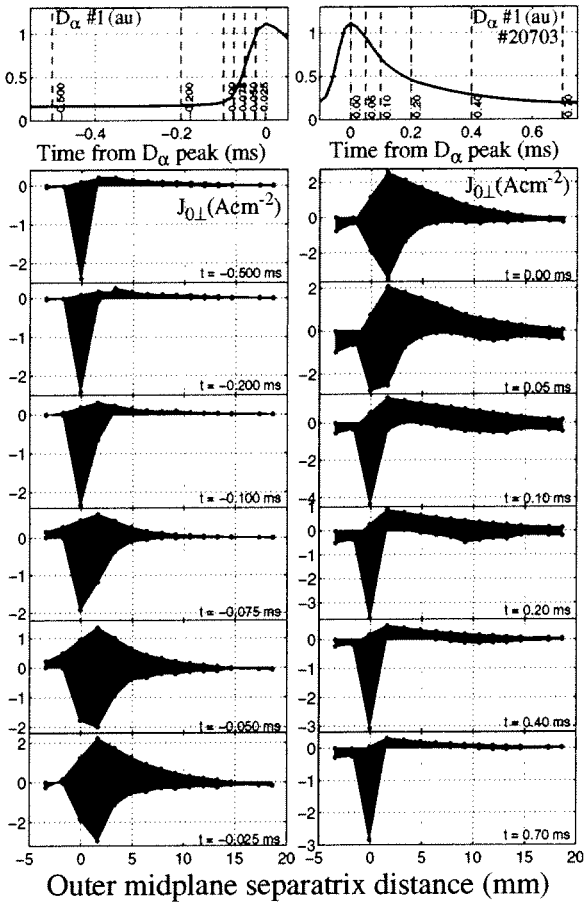


Fig. 21. Evolution of projected inner (blue) and outer (red) target current density profiles during the coherent ELM mapped to the outside midplane. To take advantage of the effective higher spatial resolution at the inner target owing to the larger flux expansion, the outer target probe data are mapped to the inner target and then linearly interpolated onto the inner probe positions. Each profile corresponds to a single time in the coherent ELM marked by the vertical lines in the top $D_\alpha$ traces.

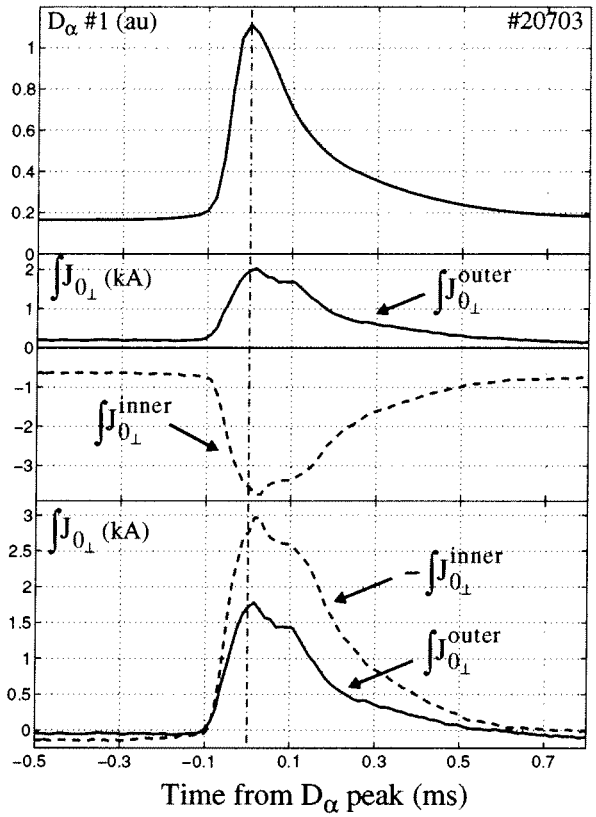


Fig. 22. Coherent average in the interval 0.5-0.8 s of the integrated perpendicular current densities to inner and outer targets, including all probes in the private flux regions with measurable current (middle panel). In the lower panel, the current offsets at t = -0.1 ms have been subtracted and the inner total current inverted to highlight the approximate factor of 2 imbalance in favour of the inner target. Subtracting the offsets in this way essentially removes the persistent strong, narrow negative current feature near the inner target strike point, thought to be a pressure related current (see text).

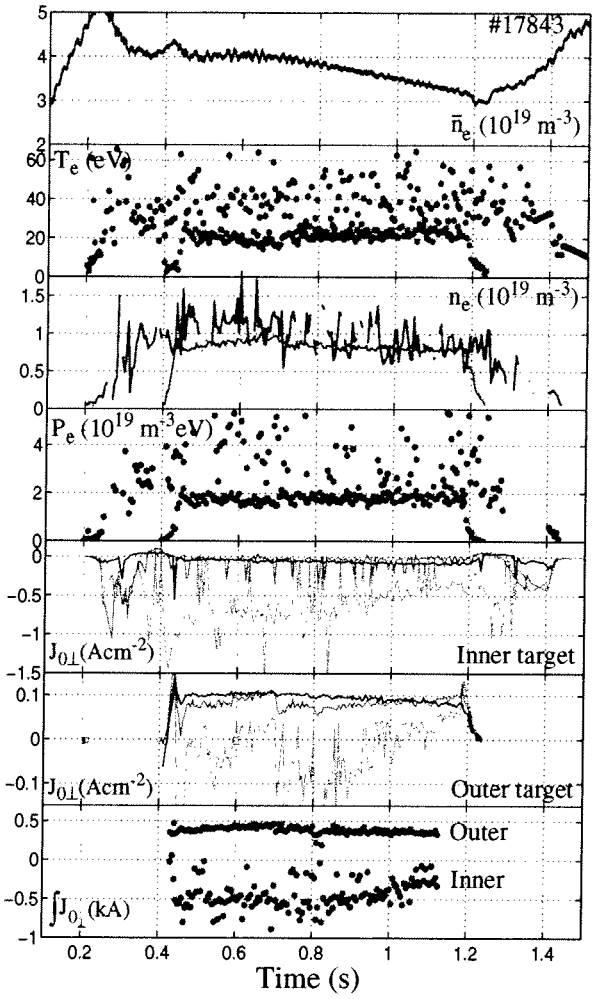


Fig. 23. Selection of target probe data for an ohmic L-mode SNL, low density (top trace) discharge with $I_p$ = 340 kA (see Fig. 24 for the equilibrium). Inner target data for $T_e$, $n_e$, $P_e$ (electron pressure) and integrated target current in red (probe #6), outer target (probe #5) in blue. The individual traces for projected current density correspond to data from the near strike point probes (#52,5 in black), from the adjacent probes on the private flux side (#53, 4 in green) and from the nearest probes on the common flux side (#51, 6 in magenta).

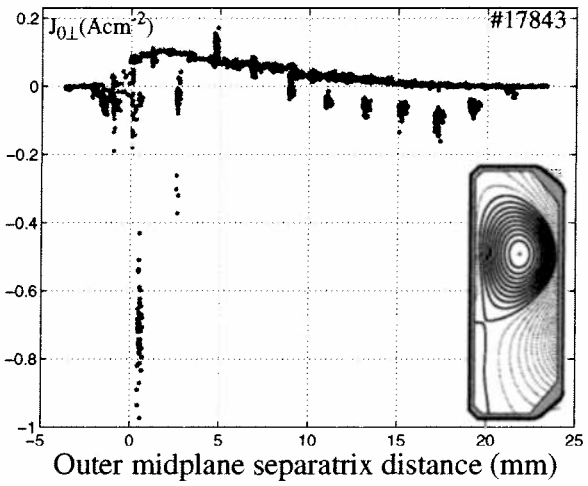


Fig. 24. Equivalent of Fig. 21 for the L-mode perpendicular current density profiles at the inner (blue) and outer (red) targets mapped to the outside midplane. All data in the interval 0.5-0.7 s are plotted with no averaging and no interpolation. In contrast to the ELM case, the higher flux expansion at the outer target in this equilibrium (see inset) now gives superior spatial resolution at the outer divertor. Note that, as in the ELM case, the uncertainty in the reconstructed strike point position and the 19 mm separation between inner target probes does not permit accurate localisation of the strong negative current feature at the inner target.